A Proposal for a Future Short-Baseline Neutrino Oscillation Program on the Fermilab Booster Neutrino Beam

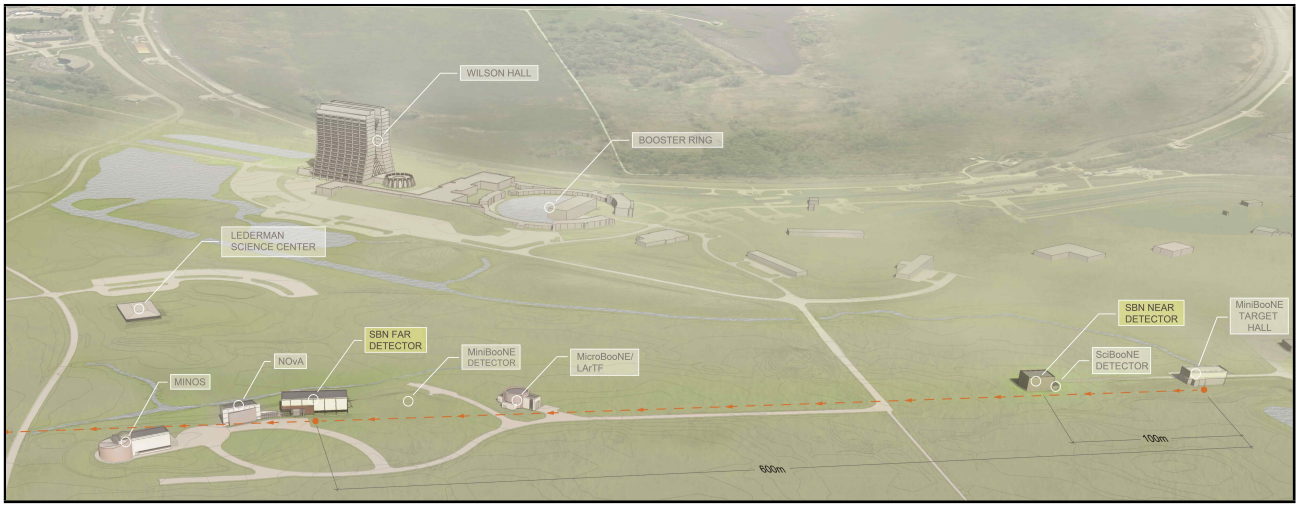

Part I: Physics Program

DRAFT
December 10, 2014

CONTENTS

I. Overview of the SBN Experimental Program 1
A. The Booster Neutrino Beam 2
B. The Detector Systems: MicroBooNE, LAr1-ND, ICARUS T600 3
C. SBL Neutrino Anomalies and The Physics of Sterile Neutrinos 6
D. The Current Experimental Landscape 9

II. SBN Oscillation Searches 12
A. Analysis Methods 12
B. Intrinsic ν_e and ν_μ Event Rates 14
C. Neutrino Flux Uncertainties 17
D. Neutrino Interaction Uncertainties 19
E. Detector Systematics 20
F. Beam-Induced "Dirt" Events 22
G. Cosmogenic Backgrounds 26
H. $\nu_\mu \to \nu_e$ Appearance Sensitivity 34
I. $\nu_\mu \to \nu_x$ Disappearance Sensitivity 39

A. Detector Volumes and Masses 41

References 41

I. OVERVIEW OF THE SBN EXPERIMENTAL PROGRAM

The future short-baseline experimental configuration is proposed to include three Liquid Argon Time Projection Chamber detectors (LArTPCs) located on-axis in the Booster Neutrino Beam (BNB) as summarized in Table I. The near detector (LAr1-ND) will be located in a new building directly downstream of the existing SciBooNE enclosure 110 m from the BNB target. The MicroBooNE detector, which is currently in the final stages of installation, is located in the Liquid Argon Test Facility (LArTF) at 470 m. The far detector (the existing ICARUS T600) will be located in a new building 600 m from the target between MiniBooNE and the NOvA near detector surface building. Figure 1 shows the locations of the detectors superimposed on an aerial view of the Fermilab neutrino experimental area. The following sections briefly describe the attributes of the three detectors; more detailed descriptions are provided in dedicated Design Reports submitted with this proposal. The initial physics studies are all based on the assumption that no modifications will be made to the existing BNB target and horn. However, studies are on-going to determine what changes could be made to the target and horn to re-optimize for LArTPC detectors and increase event rates per proton on target along the BNB.

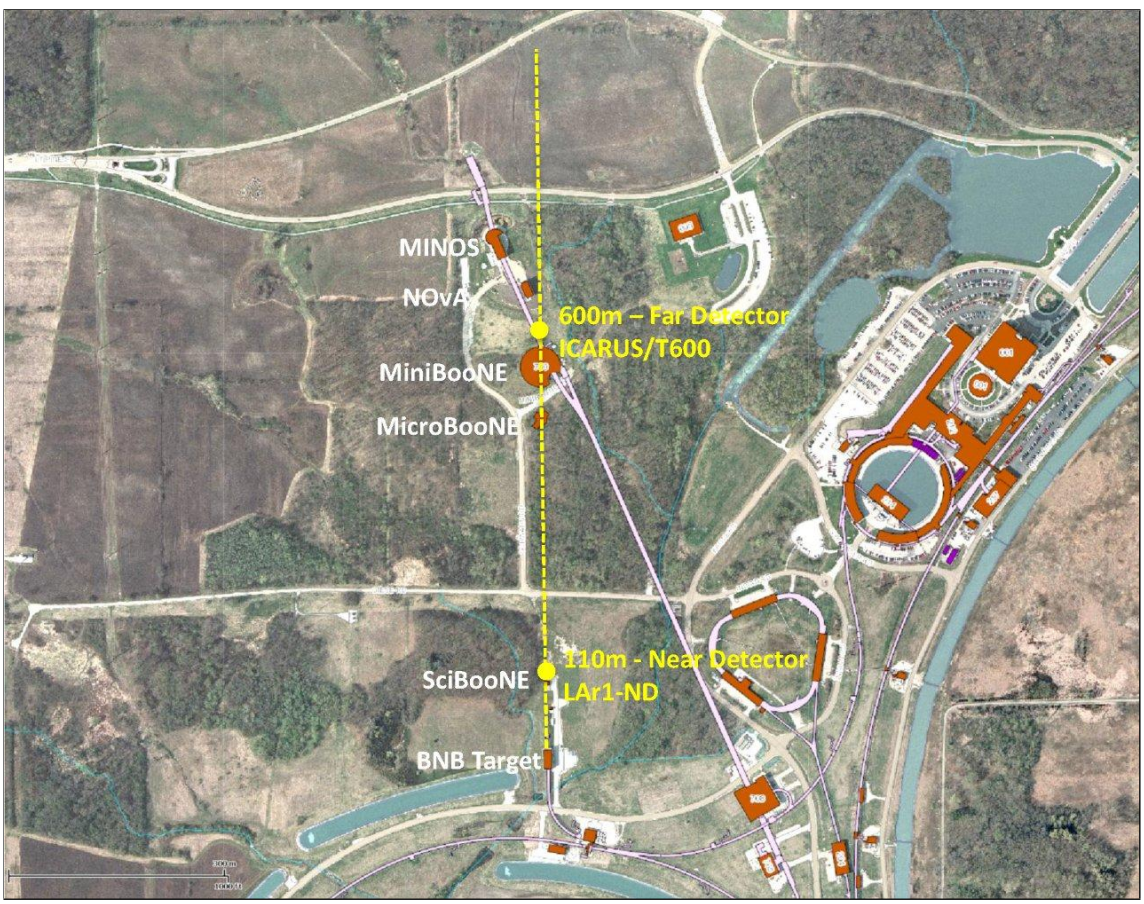

FIG. 1: *Map of the Fermilab neutrino beamline area showing the axis of the BNB (yellow dashed line) and approximate locations of the SBN detectors at 110 m, 470 m, and 600 m. The pink line indicates the axis of the NuMI neutrino beam for reference.*

Detector	Distance from BNB Target	LAr Total Mass	LAr Active Mass
LAr1-ND	110 m	220 t	112 t
MicroBooNE	470 m	170 t	89 t
ICARUS T600	600 m	760 t	476 t

TABLE I: *Summary of the SBN detector locations and masses.*

A. The Booster Neutrino Beam

The Booster Neutrino Beam is created by extracting protons from the Booster accelerator at 8 GeV kinetic energy (8.89 GeV/c momentum) and impacting them on a 1.7λ beryllium (Be) target to produce a secondary beam of hardrons, mainly pions. Charged secondaries are focused by a single toroidal aluminum alloy focusing horn that surrounds the target. The horn is supplied with 174 kA in 143 μs pulses coincident with proton delivery. The horn can be pulsed with either polarity, thus focusing either positives or negatives and de-focusing the other. Focused mesons are allowed to propagate down a 50 m long, 0.91 m radius air-filled tunnel where the majority will decay to produce muon and electron neutrinos. The remainder are absorbed into a concrete and steel absorber at the end of the 50 m decay region. Suspended above the decay region at 25 m are concrete and steel plates which can be deployed to reduce the available decay length, thus systematically altering the neutrino fluxes. A schematic of the BNB target station and decay region is shown in Figure 2. See Refs. [1, 2] for technical design reports on the 8 GeV extraction line and the Booster Neutrino Beam.

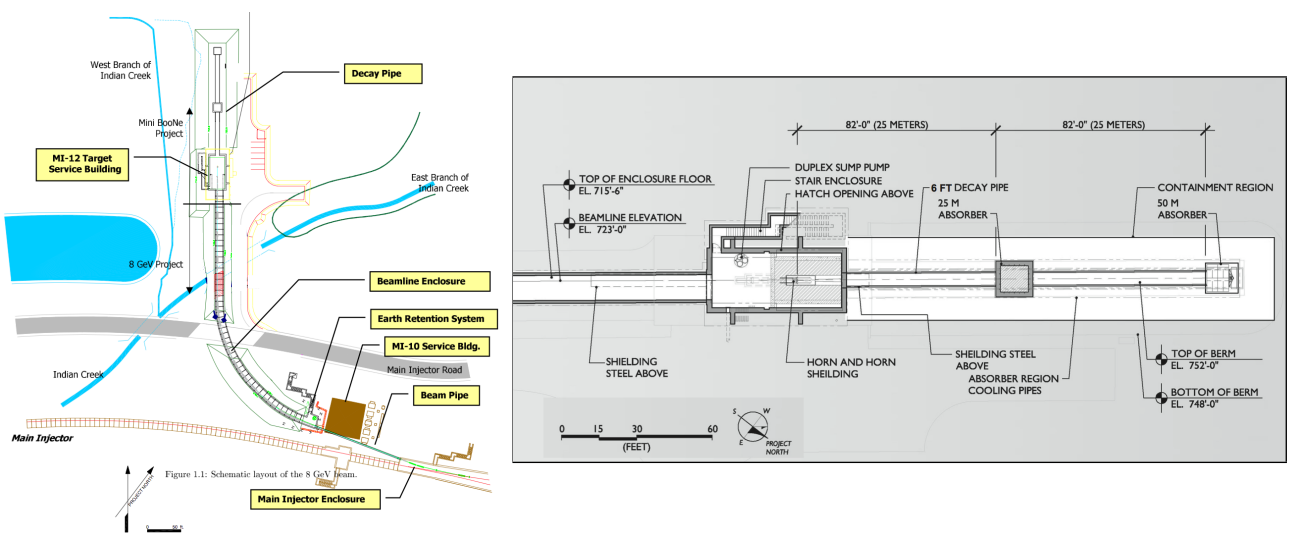

FIG. 2: *Schematic drawings of the Booster Neutrino Beamline including the 8 GeV extraction line, target hall and decay region.*

The timing structure of the delivered proton beam is an important aspect for the physics program. The Booster spill length is 1.6 μs with nominally $\sim 5\times10^{12}$ protons per spill delivered to the beryllium target. The main Booster RF is operated at 52.8 MHz, with some 81 buckets filled out of 84. The beam is extracted into the BNB using a fast-rising kicker that extracts all of the particles in a single turn. The resulting structure is a series of 81 bunches of protons each $\sim$2 ns wide and 19 ns apart. While the operating rate of the Booster is 15 Hz, the maximum

allowable average spill delivery rate to the BNB is 5 Hz, set by the design of the horn and its power supply.

The BNB has already successfully and stably operated for 12 years in both neutrino and anti-neutrino modes. The fluxes are well understood thanks to a detailed simulation [3] developed by the MiniBooNE Collaboration and the availability of dedicated hadron production data for 8.9 GeV/c p+Be interactions collected at the HARP experiment at CERN [4]. Systematic uncertainties associated with the beam have also been characterized in a detailed way as seen in Refs. [3, 5] with a total error of ∼9% at the peak of the ν_μ flux and larger in the low and high energy regions.

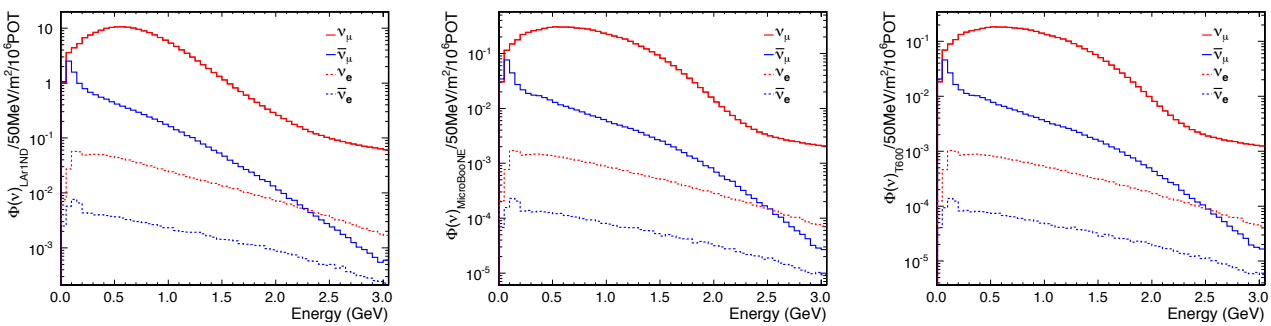

FIG. 3: *The Booster Neutrino Beam flux at the three SBN detectors: (left) LAr1-ND, (center) MicroBooNE, and (right) ICARUS T600.*

The neutrino fluxes observed at the three SBN detector locations are shown in Figure 3. Note the rate in the near detector is 20-30 times higher than at the MicroBooNE and ICARUS locations. Also, one sees the ν_μ flux is slightly broader at the far locations as a result of the larger solid angle viewed by the far detector. We'll see later, however, that this does not introduce a significant systematic in oscillation searches. The shapes of the $\nu_e/\bar{\nu}_e$ fluxes are more similar. The composition of the flux in neutrino mode (focusing positive hadrons) is dominated by ν_μ (93.6%), followed by $\bar{\nu}_\mu$ (5.9%), with an intrinsic $\nu_e/\bar{\nu}_e$ contamination at the level of 0.5%. The majority of the ν_μ flux originates from pion decay in flight ($\pi^+ \to \mu^+ + \nu_\mu$) except above ∼2 GeV where charged kaon decay is the largest contributor. A substantial portion of the intrinsic ν_e flux, 51%, originates from the pion → muon decay chain ($\pi^+ \to \mu^+ \to e^+ + \nu_e + \nu_\mu$) with the remaining portion from K^+ and K^0 decays.

B. The Detector Systems: MicroBooNE, LAr1-ND, ICARUS T600

MicroBooNE

MicroBooNE is currently in the final stages of construction and will be commissioned at the end of 2014. The experiment will measure neutrino interactions in argon for multiple reaction channels and investigate the source of the currently unexplained excess of low energy electromagnetic events observed by MiniBooNE. MicroBooNE also incorporates several important R&D features: the use of a non-evacuated cryostat, passive insulation of the cryostat and cryogenics, cold (in liquid) electronics, a long 2.56 meter drift distance, and a novel UV laser calibration system [6]. To accomplish these goals, the MicroBooNE detector is a 170 ton total mass (89 ton active mass) liquid argon TPC contained within a conventional cryostat [7]. The

active region of the TPC is a rectangular volume of dimensions 2.33 m $\times$ 2.56 m $\times$ 10.37 m. The TPC cathode plane forms the vertical boundary of the active volume on the left side of the detector when viewed along the neutrino beam direction (beam left). The MicroBooNE TPC design allows ionization electrons from charged particle tracks in the active liquid argon volume to drift 2.56 meters to a three-plane wire chamber. Three readout planes, spaced by 3 mm, form the beam-right side of the detector, with 3,456 Y wires arrayed vertically and 2,400 U and 2,400 V wires oriented at ± 60 degrees with respect to vertical. An array of 32 PMTs are mounted behind the wire planes on the beam right side of the detector to collect prompt scintillation light produced in the argon [8].

MicroBooNE is approved to receive an exposure of 6.6×10^{20} protons on target in neutrino running mode from the BNB. It will also record interactions from an off-axis component of the NuMI neutrino beam. During MicroBooNE running, the BNB will be operated in the same configuration that successfully delivered neutrino and anti-neutrino beam to MiniBooNE for more than a decade, thereby significantly reducing systematic uncertainties in the comparison of MicroBooNE data with that from MiniBooNE.

As of the writing of this document, construction of the MicroBooNE TPC has been completed and on June 23, 2014, the MicroBooNE vessel was moved to the Liquid Argon Test Facility (LArTF), a new Fermilab enclosure just upstream of the MiniBooNE detector hall. Final installation and detector commissioning has begun. MicroBooNE is on schedule to begin taking neutrino data in early 2015.

LAr1-ND

The design of the Liquid Argon Near Detector, or LAr1-ND [9], builds on many years of LArTPC detector R&D and experience from design and construction of the ICARUS T600, ArgoNeuT, MicroBooNE, and LBNF detectors. The basic concept is to construct a membrane-style cryostat in a new on-axis enclosure adjacent to and directly downstream of the existing SciBooNE hall. The membrane cryostat will house a CPA (Cathode Plane Assembly) and four APAs (Anode Plane Assemblies) to read out ionization electron signals. The active TPC volume is 4.0 m (width) $\times$ 4.0 m (height) $\times$ 5.0 m (length, beam direction), containing 112 tons of liquid argon. Figure 4 shows the state of the conceptual design for the Near Detector building and the LAr1-ND TPC.

The two APAs located near the beam-left and beam-right walls of the cryostat will each hold 3 planes of wires with 3 mm wire spacing. The APAs use the same wire bonding method developed for the LBNF APAs, but without the continuous helical wrapping to avoid ambiguity in track reconstruction. Along the common edge of neighboring APAs, the U & V wires are electrically "jumped". TPC signals are then read out with banks of cold electronics boards at the top and two outer vertical sides of each detector half. The total number of readout channels is 2,816 per APA (11,264 in the entire detector). The CPA has the same dimensions as the APAs and is centered between them. It is made of a stainless-steel framework, with an array of stainless-steel sheets mounted over the frame openings. Each pair of facing CPA and APA hence forms an electron-drift region. The open sides between each APA and the CPA are surrounded by 4 FCAs (Field Cage Assemblies), constructed from FR4 printed circuit panels with parallel copper strips, to create a uniform drift field. The drift distance between each APA and the CPA is 2 m such that the cathode plane will need to be biased at -100 kV for a nominal 500 V/cm field. The LAr1-ND design will additionally include a light collection system for detecting scintillation light produced in the argon volume.

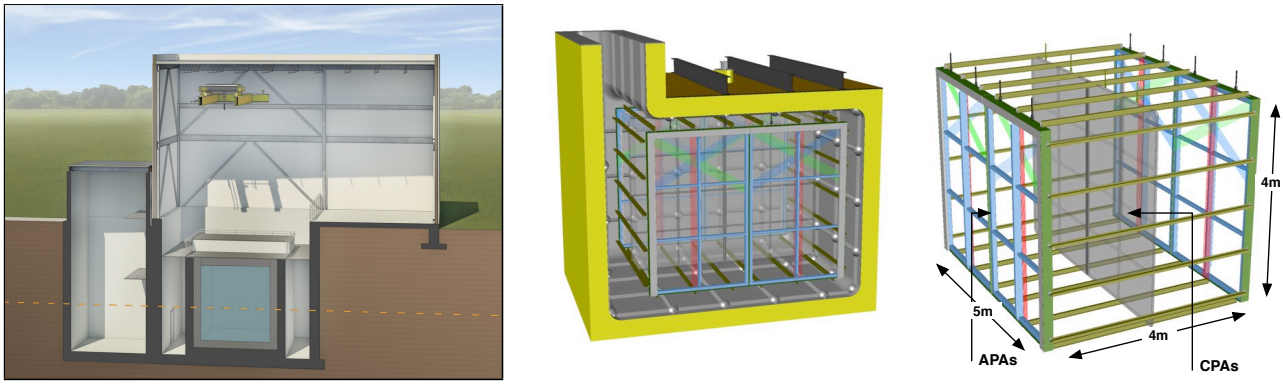

FIG. 4: *(Left) The LAr1-ND detector building concept. The neutrino beam center is indicated by the orange dashed line and enters from the left. (Right) The LAr1-ND TPC conceptual design.*

Overall, the design philosophy of the LAr1-ND detector is to serve as a prototype for LBNF that functions as a physics experiment. While the present conceptual design described here is an excellent test of LBNF detector systems sited in a neutrino beam, the LAr1-ND collaboration is exploring innovations in this design and the opportunity to further test them in a running experiment.

ICARUS T600

The ICARUS T600 detector installed in the underground INFN-LNGS Gran Sasso Laboratory has been the first large-mass LArTPC operating as a continuously sensitive general purpose observatory. The successful operation of the ICARUS T600 LArTPC demonstrates the enormous potential of this detection technique, addressing a wide physics program with the simultaneous exposure to the CNGS neutrino beam and cosmic-rays [10].

The ICARUS T600 detector consist of two large identical modules with internal dimensions $3.6 \times 3.9 \times 19.6$ m^3 filled with ~ 760 tons of ultra-pure liquid argon, surrounded by a common thermal insulation [10, 11]. Each module houses two TPCs separated by a common central cathode for an active volume of $3.2 \times 2.96 \times 18.0$ m^3. A uniform electric field ($E_D = 500$ V/cm) is applied to the drift volume. The reliable operation of the high-voltage system has been extensively tested in the ICARUS T600 up to about twice the operating voltage (150 kV, corresponding to $E_D = 1$ kV/cm). Each TPC is made of three parallel wire planes, 3 mm apart, with 3 mm pitch, facing the drift path (1.5 m) and with wires oriented at 0^0, $\pm 60^0$ with respect to the horizontal direction, respectively. Globally, 53,248 wires with length up to 9 m are installed in the detector. A three-dimensional image of the ionizing event is reconstructed combining the wire coordinate on each plane at a given drift time with $\sim$1 mm^3 resolution over the whole active volume (340 m^3 corresponding to 476 tons).

The ICARUS T600 detector is now in the process of being moved to CERN for a complete overhauling preserving most of the existing operational equipment, while upgrading some components with up-to-date technology in view of its future near surface operation. The refurbishing will include the following main activities:

- realization of new vessels for LAr containment and new thermal insulation, based on similar technology as foreseen for LBNF and the near detector;

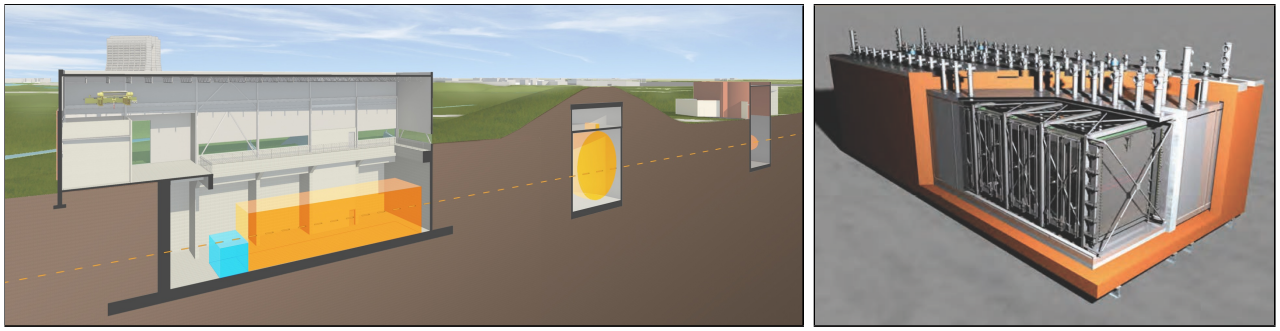

FIG. 5: *(Left) The ICARUS T600 detector building concept. The neutrino beam center is indicated by the orange dashed line and enters from the right. The existing MiniBooNE and MicroBooNE buildings are also shown. (Right) ICARUS T600 detector schematic showing both modules and the common insulation surrounding the detector.*

- implementation of an improved light collection system, to allow a more precise event localization and the disentangling of the background induced by cosmic rays;
- implementation of new readout electronics;
- realization of an anti-coincidence system to automatically tag cosmic rays crossing the LAr active volume;
- complete review and maintenance of the cryogenics and purification systems.

The above program will be carried out in the context of a joint effort of the ICARUS Collaboration and CERN. The detector is expected to be transported to FNAL beginning of 2017. Installation and operation at Fermilab will require significant involvement of Fermilab technical personnel. All of the above mentioned activities will also bring considerable value as R&D for a future long-baseline neutrino facility based on LAr.

C. SBL Neutrino Anomalies and The Physics of Sterile Neutrinos

Experimental observations of neutrino oscillations have established a picture consistent with the mixing of three neutrino flavors (ν_e, ν_μ, ν_τ) with three mass eigenstates (ν_1, ν_2, ν_3) whose differences turn out to be relatively small, with $\Delta m^2_{31} \simeq 2.4 \times 10^{-3}$ eV^2 and $\Delta m_{21} \simeq 7.5 \times 10^{-5}$ eV^2. However, in recent years, several experimental "anomalies" have been reported which, if experimentally confirmed, could be hinting at the presence of additional neutrino states with larger mass-squared differences participating in the mixing [12].

Two distinct classes of anomalies pointing at additional physics beyond the Standard Model in the neutrino sector have been reported, namely *a*) the apparent disappearance signal in low energy anti-neutrinos from nuclear reactors beyond the expected θ_{13} effect [13] (the "reactor anomaly") and from Mega-Curie radioactive neutrino sources in the Gallium experiments [14, 15] originally designed to detect solar neutrinos (the "Gallium anomaly"), and *b*) evidence for an electron-like excess in interactions coming from neutrinos from particle accelerators [16–19] (the "LSND and MiniBooNE anomalies"). None of these results can be described by oscillations between the three Standard Model neutrinos and, therefore, could be suggesting important new

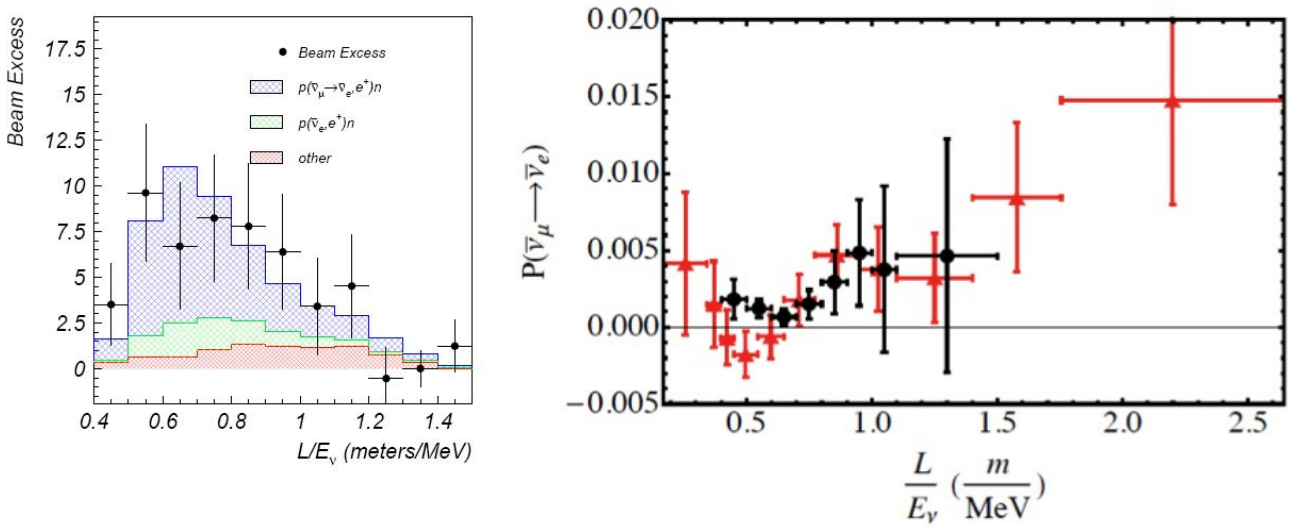

FIG. 6: *Left: Excess of electron neutrino candidate events observed by the LSND experiment [16]. Right: Oscillation probability as a function of L/E_ν if the excess candidate events are assumed to be due to $\bar{\nu}_\mu \to \bar{\nu}_e$ transitions using MiniBooNE (red) and LSND (black) data.*

physics with the possible existence of at least one fourth non-standard neutrino state, driving neutrino oscillations at a small distance, with typically $\Delta m^2_{new} \geq 0.1$ eV^2.

The "reactor anomaly" refers to the deficit of electron anti-neutrinos observed in numerous detectors a few meters away from nuclear reactors compared to the predicted rates, with $R_{\text{avg}} = N_{\text{obs}}/N_{\text{pred}} = 0.927 \pm 0.023$ [13]. The reference spectra take advantage of an evaluation of inverse beta decay cross sections impacting the neutron lifetime and account for long-lived radioisotopes accumulating in reactors [20, 21]. Recent updates have changed the predictions slightly giving a ratio $R_{\text{avg}} = 0.938 \pm 0.023$, a 2.7σ deviation from unity [22]. Moreover, some lack of knowledge of the reactor neutrino fluxes is still remaining and a detailed treatment of forbidden transitions in the reactor spectra computation may result in a few percent increase of systematic uncertainties [23]. A similar indication for electron neutrino disappearance has been recorded by the SAGE and GALLEX solar neutrino experiments measuring the calibration signal produced by intense k-capture sources of ^{51}Cr and ^{37}Ar. The combined ratio between the detected and the predicted neutrino rates from the sources is $R = 0.86 \pm 0.05$, again about 2.7 standard deviation from $R = 1$ [14, 15]. Both of these deficits of low energy electron neutrinos over very short baselines could be explained through ν_e disappearance due to oscillations at $\Delta m^2 \geq 1$ eV^2.

The LSND experiment [16] at Los Alamos National Laboratory used a decay-at-rest pion beam to produce muon anti-neutrinos between 20-53 MeV about 30 m from a liquid scintillator-based detector where $\bar{\nu}_e$ could be detected through inverse beta decay (IBD) on carbon, $\bar{\nu}_e p \to e^+ n$. After 5 years of data taking $89.7 \pm 22.4 \pm 6.0$ $\bar{\nu}_e$ candidate events were observed above backgrounds, corresponding to 3.8σ evidence for $\bar{\nu}_\mu \to \bar{\nu}_e$ oscillations [16] occurring at a Δm^2 in the 1 eV^2 region. This signal, therefore, cannot be accommodated with the three Standard Model neutrinos, and like the other short-baseline hints for oscillations at $L/E_\nu \sim$1 m/MeV, implies new physics.

The MiniBooNE experiment at Fermilab measured neutrino interactions 540 m from the target of the Booster Neutrino Beam (BNB), a predominantly muon neutrino beam peaking at 700 MeV. Muon and electron neutrinos are identified in charged-current interactions by the characteristic signatures of Cherenkov rings for muons and electrons. In a ten year data set

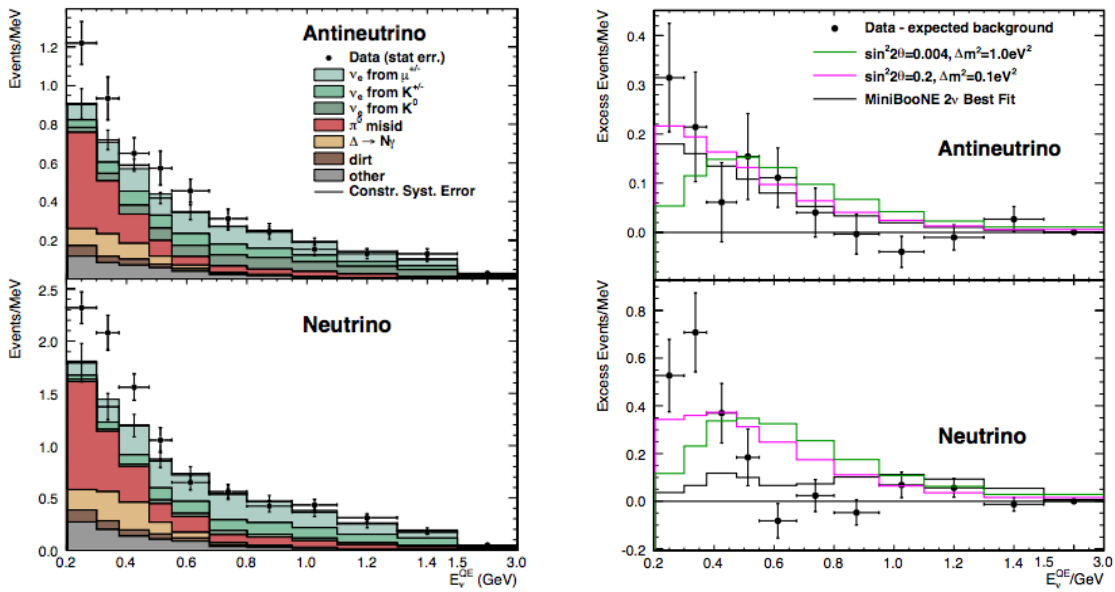

FIG. 7: *Left: $\bar{\nu}_e$ (top) and ν_e (bottom) candidate events and predicted backgrounds showing the observed excesses in the MiniBooNE data. Right: background subtracted event rates in the MiniBooNE anti-neutrino (top) and neutrino (bottom) data [19]. E_ν^{QE} refers to the reconstructed neutrino event energy, where a quasi-elastic interaction is assumed in the reconstruction.*

including both neutrino and anti-neutrino running [17–19, 24], MiniBooNE has observed a 3.4σ signal excess of ν_e candidates in neutrino mode (162.0 ± 47.8 electromagnetic events) and a 2.8σ excess of $\bar{\nu}_e$ candidates in anti-neutrino mode (78.4 ± 28.5 electromagnetic events) as shown in Figure 7. Figure 6 compares the L/E_ν dependence of the MiniBooNE anti-neutrino events to the excess observed at LSND. The excess events can be electrons or single photons since these are indistinguishable in MiniBooNE's Cherenkov imaging detector. MicroBooNE will address this question at the same baseline as MiniBooNE by utilizing the added capability to separately identify electrons and photons.

An important contribution to the sterile neutrino search has been made by the ICARUS Collaboration with the T600 detector running in the underground INFN-LNGS Gran Sasso Laboratory and exposed to the CERN to Gran Sasso (CNGS) neutrino beam [10]. Although not testing fully the relevant space of oscillation parameters, ICARUS results, corroborated by the OPERA experiment [25], limit the window for the LSND anomaly to a narrow region around $\Delta m^2 \sim 0.5$ eV^2 and $\sin^2 2\theta \sim 0.005$ [26], [27]. In this region, there is overall agreement between the present ICARUS limit, the limit from the KARMEN experiment [28], and the positive signals of LSND and MiniBooNE.

The most common interpretation of this collection of data is evidence for the existence of one or more additional, mostly "sterile" neutrino states with masses at or below the few eV range. The minimal model consists of a hierarchical 3+1 neutrino mixing, acting as a perturbation of the standard three-neutrino model dominated by the three ν_e, ν_μ and ν_τ active neutrinos with only small contributions from sterile flavors. The new sterile neutrino would mainly be composed of a heavy neutrino ν_4 with mass m_4 such that the new $\Delta m^2 = \Delta m^2_{41}$ and $m_1,\ m_2,\ m_3 \ll m_4$ with $\Delta m^2_{41} \approx [0.1 - 10]$ eV^2.

In the 3+1 minimal extension to the Standard Model, the effective ν_e appearance and ν_μ

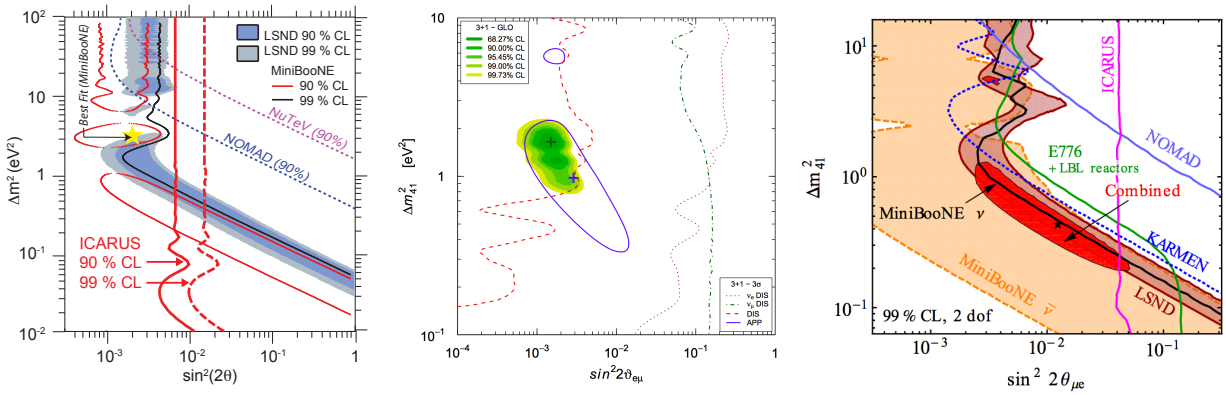

FIG. 8: *(Left) The main published experimental results sensitive to $\nu_\mu \to \nu_e$ at large Δm^2 [16–19, 28–31] including the present ICARUS limit [27] from the run in Gran Sasso. Global analysis of short-baseline neutrino results from Giunti et al. [32] (center) and Kopp et al. [33] (right). The blue closed contour on the left and the red solid area on the right are the allowed parameter regions for $\overset{(-)}{\nu}_\mu \to \overset{(-)}{\nu}_e$ appearance data and both indicate preferred Δm^2_{41} values in the ∼[0.2–2] eV^2 range.*

disappearance probabilities are described by:

$$P^{3+1}_{\nu_\alpha \to \nu_\beta} = \delta_{\alpha\beta} - 4\,|U_{\alpha 4}|^2 \left(\delta_{\alpha\beta} - |U_{\beta 4}|^2\right) \sin^2\left(\frac{\Delta m^2_{41} L}{4E_\nu}\right) \tag{1}$$

where U_{ij} are elements of the now 4×4 mixing matrix and L is the travel distance of the neutrino of energy E_ν. The interpretation of both the LSND and MiniBooNE anomalies in terms of light sterile neutrino oscillations requires mixing of the sterile neutrino with both electron and muon neutrinos. Constraints on sterile neutrino mixing from ν_μ and neutral-current disappearance data are also available. An explanation of all the available observations in terms of oscillations suffers from significant tension between appearance and disappearance data, particularly due to the absence of ν_μ disappearance in the $\Delta m^2 \sim 1$ eV^2 region. Many global analyses of experimental results have been performed fitting to models including one or more sterile neutrinos. Figure 8 shows two recent examples [32, 33] of fits to a 3+1 model which indicate similar allowed parameter regions in the $\Delta m^2_{41} \approx [0.2 - 2]$ eV^2 range when considering available $\nu_e/\bar{\nu}_e$ appearance data. Later, in Section II A, we will compare SBN sensitivity predictions to the original LSND allowed region and the allowed parameter space in the global data fit from Kopp et al. [33] (the red combined region from Figure 8, right) and Giunti et al. [32] (the green combined region from Figure 8, center).

D. The Current Experimental Landscape

Given the importance of a sterile neutrino discovery, it is clear that the existing anomalies must be explored further by repeating the existing measurements in an effective way capable of addressing the oscillation hypothesis and many experiments are setting out to explore it [34].

New reactor experiments searching for oscillations with $L/E_\nu \sim 1$ m/MeV are in preparation aiming to detect an oscillation pattern imprinted in the energy distribution of events. Experimentally the detection technique relies on the IBD reaction, $\bar{\nu}_e p \to e^+ n$, where the positron

carries out the $\bar{\nu}_e$ energy and tagging the neutron provides a discriminant signature against backgrounds. The backgrounds from radioactive contaminants or induced by the reactor core and by cosmic rays can partially be suppressed through passive shielding while the remaining contribution can be measured in-situ at the analysis stage. The Nucifer experiment [35] at the Osiris nuclear reactor in Saclay could provide first new constraints by 2015. The Stereo experiment [36] will be constructed next to the ILL reactor in Grenoble, France. The DANSS [37] and Neutrino4 [38] experiments are under construction in Russia and should provide first data in 2015. Finally, comprehensive projects for searching for sterile neutrinos at reactors in China [39] and the US [40] are currently under study. All these experiments are designed to test the space of oscillation parameters deduced from the interpretation of the reactor anti-neutrino deficits.

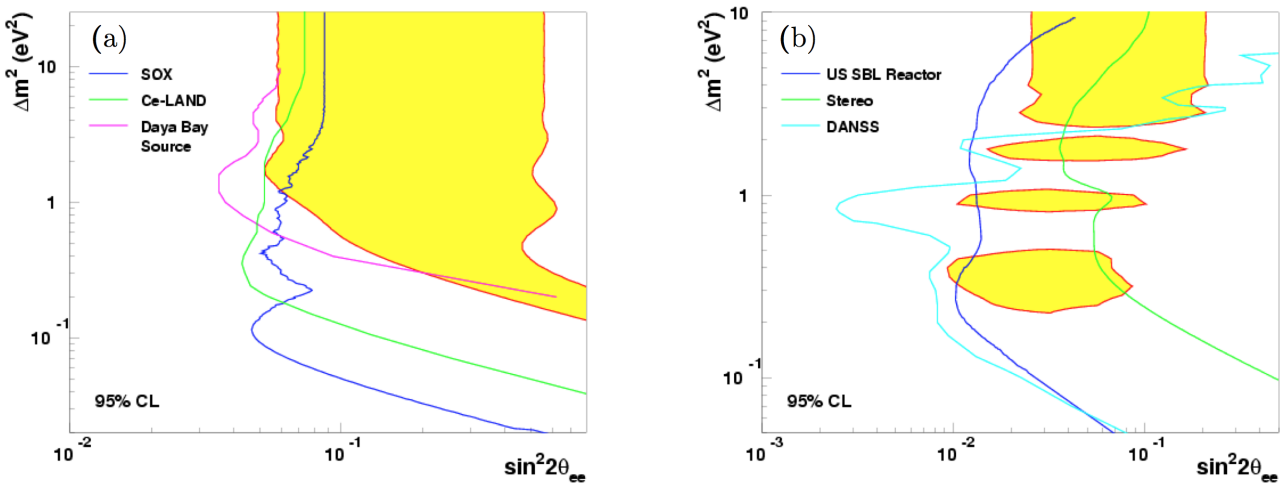

FIG. 9: *Expected sensitivity curves at 95% C.L. for proposed neutrino experiments with radioactive sources (a) and reactors (b) with the global fits to the existing gallium and reactor data (yellow regions) [41].*

New projects aiming to search for evidence of oscillations using neutrinos from intense radioactive sources have also been proposed. The SOX experiment [42] will perform such a measurement with a 10 MCi ^{51}Cr source deployed at 8.25 m from the center of the Borexino detector in 2017. At Baksan a 3 MCi ^{51}Cr source could be placed at the center of a target, containing 50 tons of liquid metallic gallium divided into two areas, an inner 8 ton zone and an outer 42 ton zone. The ratio of the two measured capture rates to its expectation could signify an oscillation. This is a well-proven technique free of backgrounds, developed for the SAGE solar neutrino experiment. The CeLAND and CeSOX projects plan to use 100 kCi of ^{144}Ce in KamLAND [43, 44] and Borexino [42, 43] to produce an intense anti-neutrino flux which can be detected through the inverse beta decay process. The goal is to deploy the ^{144}Ce radioisotope about 10 m away from the detector center and to search for an oscillating pattern in both event spatial and energy distributions that would determine neutrino mass differences and mixing angles unambiguously. The CeSOX experiment could take data as early as the end of 2015 at LNGS with Borexino.

A new neutrino, ν_4, heavier than the three active neutrinos should be detected in the KATRIN experiment [45]. The detector aims as measuring precisely the high energy tail of the tritium β-decay spectrum by combining an intense molecular tritium source with an integrating high-resolution spectrometer reaching a 200 meV sensitivity on the effective electron neutrino

mass at 90% C.L. The detection principle for a new sterile neutrino state is to search for a distortion at the high energy endpoint of the electron spectrum of tritium β-decay, since its shape is *a priori* very precisely understood. The KATRIN experiment can probe part of the current allowed region of the reactor anti-neutrino anomaly, especially for $\Delta m^2_{new} > 1$ eV^2, with 3 years of data-taking [46, 47]. First results are expected in 2016.

As a long term project, a huge statistics of $\bar{\nu}_\mu$ from the β-decay of ^{8}He could be obtained through the development of a high-power low energy cyclotron. The IsoDAR project [48] proposes to place such a device underground in the Kamioka mine to search for an oscillation pattern in the KamLAND detector. This would be a disappearance experiment directly testing both the reactor and the gallium anomalies starting from a well known $\bar{\nu}_\mu$ spectrum.

The OscSNS project [49] proposes to locate an 800-ton gadolinium-doped scintillator detector 60 m away from the Spallation Neutron Source (SNS) at the Oak Ridge National Laboratory in order to directly test the LSND results. This kind of facility has the advantage of producing a well-understood source of electron and muon neutrinos from π^+ and μ^+ decays-at-rest. The main search channel would be the appearance of $\bar{\nu}_e$, taking advantage of the low duty factor of SNS to reduce cosmic induced backgrounds.

A precision sterile neutrino search has been proposed with a clean and well-understood beam of ν_e and $\bar{\nu}_\mu$ produced in a low energy neutrino factory by the decay of stored muons both at CERN [50] and Fermilab [51] by the nuSTORM project. Such a neutrino beam could be used to probe both appearance and disappearance processes including the golden channel of ν_μ appearance in a muon-free electron neutrino beam, which is not possible in a meson decay-in-flight beam.

However, considering the present experimental scenario, an accelerator-based neutrino beam facility provides the best opportunity for a rich oscillation research program with a single experiment, where the existence of an oscillation signal in ν_e appearance and disappearance modes as well as ν_μ disappearance can be simultaneously investigated. Neutrino or anti-neutrino beams can be produced in the same experiment and, at accelerator beam energies, both charged-current and neutral-current channels can be explored. This is the approach of the short-baseline neutrino oscillation program on the FNAL Booster Neutrino Beam proposed here. MicroBooNE is blazing the trail on the BNB with liquid argon technology now, but the challenge of predicting absolute neutrino fluxes in accelerator beam experiments and the large uncertainties associated with neutrino-nucleus interactions, strongly motivate the use of multiple detectors at different baselines to reduce systematic uncertainties in the search for oscillations. The anomalous short-baseline results discussed in Section I C may be hinting at neutrinos oscillating with an amplitude 10 to 100 times *smaller* than the θ_{13} signals in experiments like Daya Bay, T2K, or MINOS, all multiple detector experiments. The Fermilab SBN Program, using detectors at different distances from the BNB source, will cover at high confidence level the entirety of the sterile neutrino parameter space suggested by the anomalies.

Finally, the observed set of anomalous results in neutrino physics call for conclusive new experiments capable of exploring the indicated parameter regions in a definitive way and to clarify the possible existence of eV-scale sterile neutrinos. The accelerator-based short-baseline program presented in this proposal is the only means of testing the sterile neutrino picture through multiple channels in a single beam.

II. SBN OSCILLATION SEARCHES

The SBN program of three LArTPC detectors along the Fermilab Booster Neutrino Beam delivers a rich and diverse physics opportunity. Neutrino-argon cross sections can be studied first in MicroBooNE and later with even higher statistics in LAr1-ND using the well characterized neutrino fluxes of the BNB [3]. MicroBooNE and ICARUS will record samples of higher energy events, useful for LBNF, from the off-axis NuMI beam. The source of the MiniBooNE electromagnetic event excess will be directly checked in the same beam using the LArTPC technology in order to separate $e^{\pm}$ from single γ interactions. Finally, of course, multiple detectors at different baselines allows a general, sensitive search for neutrino oscillations in multiple channels. These constitute the flagship measurements of the SBN program, and so we dedicate this Section to a careful and detailed description of the sensitivity analysis for $\nu_\mu \to \nu_e$ appearance and $\nu_\mu \to \nu_x$ disappearance.

In Section II A we provide a mathematical description of the analysis methods used to calculate the sensitivities. In Section II B we describe the procedures for selecting events for the ν_μ and ν_e analyses and characterize the in-detector intrinsic beam-related backgrounds to each. In Sections II C and II D we present the systematic uncertainties impacting these predictions related to the neutrino fluxes and neutrino interaction model, with particular emphasis on the correlations between different detector locations that enable the increased sensitivity of a multi-detector experiment. Section II E discusses detector related systematic uncertainties. Section II F deals with out-of-detector but beam-induced backgrounds; these include neutrino interactions in the earth surrounding each detector building, hence we often refer to this category as "dirt" events, though interactions in the the building, cryostat, and inactive argon surrounding the TPC which deposit energy in the detector are all included. In II G we discuss cosmogenic backgrounds and the strategies to mitigate them. Both the dirt and cosmogenic backgrounds only effect the ν_e analysis. Finally, we bring it all together and present the oscillation sensitivities of the SBN program to $\nu_\mu \to \nu_e$ appearance and $\nu_\mu \to \nu_x$ disappearance in Sections II H and II I, respectively.

A. Analysis Methods

The sensitivity of the SBN program will be demonstrated using the commonly assumed framework of three active and one sterile neutrino, or a "3+1 model", as our baseline for evaluation. Of course, other models could be assumed, such as those with multiple sterile states, but this choice provides a straight-forward way to compare to previous experimental results as well as to global data fits that were analyzed using the 3+1 model[1]. In the 3+1 model, the effective oscillation probabilities are described by Eq 1, reproduced here explicitly for ν_e appearance ($\nu_\mu \to \nu_e$) and ν_μ disappearance ($\nu_\mu \to \nu_\mu$):

$$P^{3+1}_{\nu_\mu \to \nu_e} = \sin^2 2\theta_{\mu e} \sin^2\left(\frac{\Delta m^2_{41} L}{4E_\nu}\right) \qquad P^{3+1}_{\nu_\mu \to \nu_\mu} = 1 - \sin^2 2\theta_{\mu\mu} \sin^2\left(\frac{\Delta m^2_{41} L}{4E_\nu}\right)$$

with L the propagation length of the neutrino and E_ν the neutrino energy, $\sin^2 2\theta_{\mu e} \equiv 4|U_{\mu 4} U_{e4}|^2$ is an effective mixing amplitude that depends on the amount of mixing of both ν_μ and ν_e with

[1] Of course, what we would like to know is the general ability of the experiment to observe either an excess or a deficit relative to the expectation in the absence of any oscillation. In a sense, the 3+1 sensitivity contains this information, but for many different possible distributions of the signal events across the observed energy spectrum.

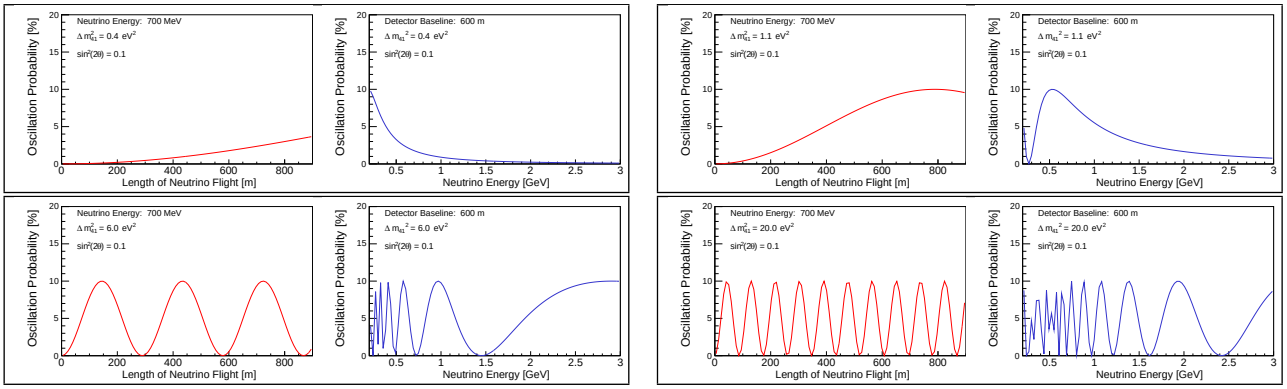

FIG. 10: *Illustrations of the oscillation probability at SBN for four different value of Δm^2_{41} in a 3+1 sterile neutrino model: Δm^2_{41} = 0.4 eV^2 (upper left), 1.1 eV^2 (upper right), 6 eV^2 (lower left), and 20 eV^2 (lower right). In each panel, the left red curve shows the evolution of the probability with* distance *at a fixed energy (E_ν = 700 MeV). The right blue curve shows the probability versus* energy *at a fixed location (600 m, the ICARUS T600 location).*

mass state ν_4, and $\sin^2 2\theta_{\mu\mu} \equiv 4|U_{\mu 4}|^2(1-|U_{\mu 4}|^2)$ only depends on the amount of ν_μ–ν_4 mixing. In our standard picture, any observation of ν_e appearance due to oscillations must be accompanied by some amount of ν_μ disappearance as well as for the similar ν_e disappearance.

Figure 10 illustrates the oscillation probability in the SBN experiments for four different possible values of Δm^2_{41}. The red curves show the evolution of the oscillation probability with distance for a fixed neutrino energy, E_ν = 700 MeV, while the blue curves demonstrate the oscillation probability across the full BNB neutrino energy range at the far detector location, 600 m. From the top row (0.4 eV^2 and 1.1 eV^2), one can clearly see why the sensitivity increases with Δm^2 up to and a little beyond 1 eV^2 as the oscillation probability at 600 m increases but also shifts toward the peak of the BNB flux. Also, note that the level of signal at the near detector location (110 m) is very small, making the near detector measurement an excellent constraint on the intrinsic beam content. For Δm^2 much larger than 1 eV^2, as we see in the bottom row (6 eV^2 and 20 eV^2), the oscillation wavelength becomes short compared to the 600 m baseline. As a function of energy in *all* detectors, the oscillations are rapid in neutrino energy and one observes an overall excess (or deficit) at all energies equal to half the value of $\sin^2 2\theta$. Therefore, at high Δm^2, the near detector is also contaminated with signal and absolute normalization uncertainties become important in determining the sensitivity.

The sensitivity is calculated by computing a χ^2 surface in the (Δm^2_{41}, $\sin^2 2\theta$) oscillation parameter plane according to:

$$\chi^2(\Delta m^2_{41}, \sin^2 2\theta) = \sum_{i,j} \left[N_i^{null} - N_i^{osc}(\Delta m^2_{41}, \sin^2 2\theta)\right] (E_{ij})^{-1} \left[N_j^{null} - N_j^{osc}(\Delta m^2_{41}, \sin^2 2\theta)\right] \quad (2)$$

where N_i^{null} is the expected event distribution in the absence of oscillations and $N_i^{osc}(\Delta m^2_{41}, \sin^2 2\theta)$ is the event prediction for an oscillation signal determined by Eq. 1 with mass splitting Δm^2_{41} and amplitude $\sin^2 2\theta$. The labels i and j indicate bins of reconstructed neutrino energy. Uncertainties, both statistical and systematic, are encoded in the covariance matrix, E_{ij}. From this surface, sensitivity contours at different confidence levels (C.L.)[2] can be identified based

[2] $\Delta\chi^2_{90} = 1.64, \Delta\chi^2_{3\sigma} = 7.74$, and $\Delta\chi^2_{5\sigma} = 23.40$ corresponding to a one-sided, one degree of freedom $\Delta\chi^2$ cut.

on the χ^2 values relative to the overall minimum value. We devote the next five Sections to describing how we estimate the background event vectors N_i^{null} and the covariance matrices E_{ij} for the ν_e appearance and ν_μ disappearance analyses.

The total systematic covariance matrix is a combination of independent matrices constructed for each of the systematic uncertainties considered:

$$E^{\text{syst}} = E^{\text{flux}} + E^{\text{cross section}} + E^{\text{cosmic bkgd}} + E^{\text{dirt bkgd}} + E^{\text{detector}} \tag{3}$$

and $E^{total} = E^{\text{stat}} + E^{\text{syst}}$ where E^{stat} is the completely uncorrelated statistical error matrix, $E_{ii}^{stat} = N_{ii}^{null}$. The flux and neutrino cross section covariance matrices are calculated using detailed Monte Carlo simulations based on GEANT4 and the GENIE neutrino event generator, respectively. Reweighting techniques are used to construct possible variations on the event distributions due to uncertainties on the underlying parameters in the models. $\mathcal{N}$ such "universes" can be combined to construct the covariance matrix:

$$E_{ij} = \frac{1}{\mathcal{N}} \sum_{m=1}^{\mathcal{N}} [N_{\text{CV}}^i - N_m^i] \times [N_{\text{CV}}^j - N_m^j], \tag{4}$$

where i and j correspond to neutrino energy bins *across all three detectors*, N_{CV} is the number of entries in each energy bin of the nominal event distribution, and N_m is the number of entries in the mth "universe". E_{ij} is the total covariance matrix, sometimes called the total error matrix, with matrix element units of (events)^2. The fractional covariance matrix is generally a more useful result and is defined as

$$F_{ij} = \frac{E_{ij}}{N_{\text{CV}}^i N_{\text{CV}}^j}. \tag{5}$$

From E_{ij} can also be extracted the correlation matrix,

$$\rho_{ij} = \frac{E_{ij}}{\sqrt{E_{ii}}\sqrt{E_{jj}}} \qquad [-1 \leq \rho \leq 1], \tag{6}$$

where ρ_{ij} describes the level of correlation between bins i and j of the neutrino energy distributions.

The flux and cross section error matrices have been constructed according to Eq. 4, while the cosmic background and dirt background error matrices are constructed differently as will be explained in the relevant Sections below.

B. Intrinsic ν_e and ν_μ Event Rates

We begin with a discussion of beam-induced neutrino interactions within the TPC active volumes that are selected when isolating ν_e and ν_μ charged-current events samples for analysis.

Electron Neutrino Charged-Current Candidates

Electron neutrino event candidates include intrinsic ν_e charged-current (CC) interactions as well as other beam-related (mostly ν_μ-induced) mis-identification backgrounds. The event selection algorithms are given below and are applied identically to all three detectors in the analysis.

A full GEANT simulation of GENIE produced neutrino interactions in argon is used and selections are made based on predicted event kinematics. As a cross-check, neutrino interactions in the ICARUS T600 detector have been also independently simulated using FLUKA[52–54], and consistent results were found. The efficiencies applied to different event types are based on inputs from other simulation results, hand-scanning studies of both simulated and real events in different detectors, and analysis results from LArTPC experiments (e.g. ICARUS, ArgoNeuT).

1. **Intrinsic/Signal ν_e CC :** ν_e charged-current interactions producing an electron with $E_e > 200$ MeV are accepted with an assumed 80% identification efficiency in our baseline sensitivity analysis. The 200 MeV shower threshold is applied to ensure good event reconstruction and identification. The simulation estimates this requirement sacrifices ∼30% of the events in the 200-350 MeV reconstructed neutrino energy bin and less than 5% above 350 MeV. It must noted, however, that the threshold for analysis of events in LAr should be well below this and lower energy events will be studied in the SBN experiments. The 80% efficiency is informed by hand-scanning exercises of simulated events in LArTPCs and significant effort is currently on-going to verify this performance with automated reconstruction algorithms. Stricter requirements on ν_e CC event selection have been discussed in the context of rejecting cosmogenic backgrounds (such as requiring visible hadronic energy at the vertex, a clear indicator of a $\nu + N$ interaction), but other handles on cosmogenic event rejection will likely deem this unnecessary (see Section II G). Also, selection efficiencies can depend on specific detector performance parameters. For instance, scanning exercises in the ICARUS detector indicate that the efficiency for recognizing isolated electron showers after the vertex is reduced ∼12% if only one 2-D view (collection) out of three is available for a complete event reconstruction (e.g. due to low signal-to-noise in the induction views). It will be important to carefully monitor such effects. Selected intrinsic ν_e CC candidates are shown in the green histograms in Figure 11.

2. **NC γ production :** Photons creating a shower above the 200 MeV selection threshold can fake the ν_e CC signature described above. For example, neutral-current interactions with any number of π^0 in the final state or radiative resonance decays are sources of such γ's. These events are analyzed according to the following criteria:

   - Second photon cut: If the second photon from a π^0 decay (with $E_\gamma > 100$ MeV as an observation threshold) converts within the TPC active volume, the event is rejected.
   - Conversion gap cut: If the neutrino interaction is inside the active volume and produces more than 50 MeV of charged hadronic activity at the vertex, then the vertex is deemed visible. With a visible vertex, if all photon showers convert more than 3 cm from that vertex, the event is rejected.
   - dE/dx cut: For events passing the previous two cuts, a 94% photon rejection rate is applied, corresponding to the expected power of separating e/γ showers in the LArTPC using the energy deposited in the first few centimeters of an electromagnetic shower.

   Beam-related photon backgrounds are shown as the orange histograms in Figure 11 labeled "NC Single γ".

3. **ν_μ CC :** ν_μ charged-current interactions with an identified primary electromagnetic (e.m.) shower within the fiducial volume could also be mis-identified as ν_e interactions if the muon

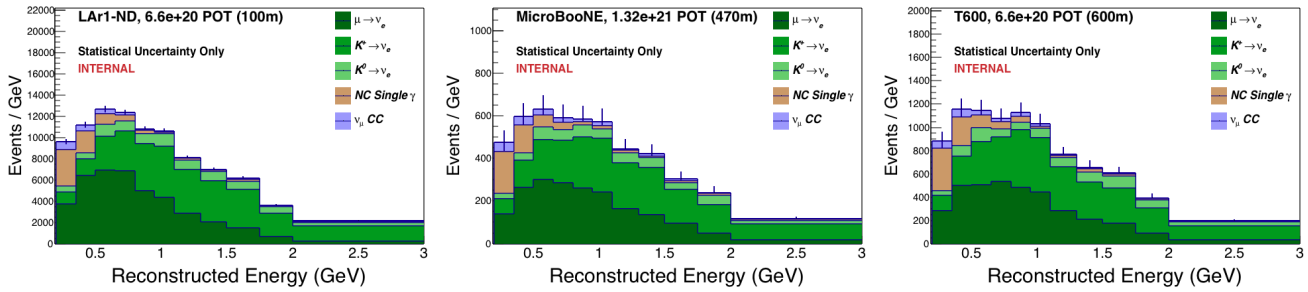

FIG. 11: *Beam-related electron neutrino charged-current candidate events in LAr1-ND (left), MicroBooNE (center), and ICARUS T600 (right). Statistical uncertainties only are shown. Data exposures are indicated on the plots and assume inclusion of the full MicroBooNE data set.*

is not identified. Minimum ionizing tracks longer than 1 m in BNB events are essentially all muons, so events with $L_\mu \geq 1$ m are rejected. Events with $L_\mu < 1$ m and a single e.m. shower attached to the CC event vertex could be identified as a $\mu + \gamma$ (ν_μ CC) or $\pi + e$ (ν_e CC) final state. We, therefore, check for the presence of candidate e.m. showers in ν_μ CC interactions following the same criteria as for NC γ events described above, and if not rejected we retain the event as a background for the ν_e CC sample. These are represented by the blue histograms in Fig. 11.

4. **Neutrino Electron Scattering :** Neutrinos can scatter off an orbiting electron in an atom, ejecting the electron at high energy. Experimentally, the signature is a very forward going electron and nothing else in the event, which mimics a ν_e charged current interaction and will be selected with the same efficiency. However, the $\nu + e$ cross section is very low and so forms a secondary background. These are too small to be seen in Figure 11 but are included in the analysis.

For estimating these background rates, the full GEANT simulation of events is important. By analyzing the conversion points of photons instead of just the true neutrino interaction vertex, we accurately account for acceptance effects in the differently shaped detectors. Because the e/γ separation is performed entirely with the first few centimeters of a shower, differences in total shower containment do not affect the assumption that the photon identification efficiency should be the same in each detector.

To simulate calorimetric energy reconstruction, the incoming neutrino energy in each Monte Carlo event is estimated by summing the energy of the lepton (or the γ faking an electron) and all charged hadrons above observation thresholds present in the final state. This approach is used in the analysis of both ν_e and ν_μ charged-current events described next. It should be noted that this method is one possible approach to estimating the neutrino energy. The liquid argon TPC technology enables a full calorimetric reconstruction, but other methods can be used as well, such as isolating charged-current quasi-elastic (CCQE) events and assuming QE kinematics. The ability to apply complementary approaches to event identification and energy reconstruction will provide valuable cross checks of the measurements performed. The stacked beam-related backgrounds to the ν_e analysis are summarized in Figure 11 as a function of the calorimetric reconstructed energy for each of the SBN detectors.

Muon Neutrino Charged-Current Candidates

Muon neutrino charged-current events are selected assuming an 80% reconstruction and identification efficiency. The only background contribution considered comes from neutral-current charged pion production, where the $\pi^{\pm}$ can be mistaken for a $\mu^{\pm}$. Simulations show pion tracks produced in the BNB are short with essentially no charged pions traveling more than a meter in the liquid argon. We, therefore, apply the simple cut of requiring a track longer than 50 cm in the event for the ν_μ CC selection. More sophisticated methods to separate pions and muons stopping in LAr are being explored, but this selection is sufficient for the current analysis. The resulting contamination from NC events is shown in Figure 12 and has a negligible impact on the oscillation sensitivity. Measurement resolutions have been introduced for this analysis by smearing both the reconstructed muon energy and hadron energy in the event and $E_\nu = E_\mu + E_{\text{had-visible}}$. The smearing of the muon energy changes depending on if the muon is fully contained within the active volume or if it exits the active volume with a minimum track length of 1 m and the energy must be estimated via the multiple scattering of the track. The distributions of selected muon neutrino charged-current events in each detector are shown in Figure 12.

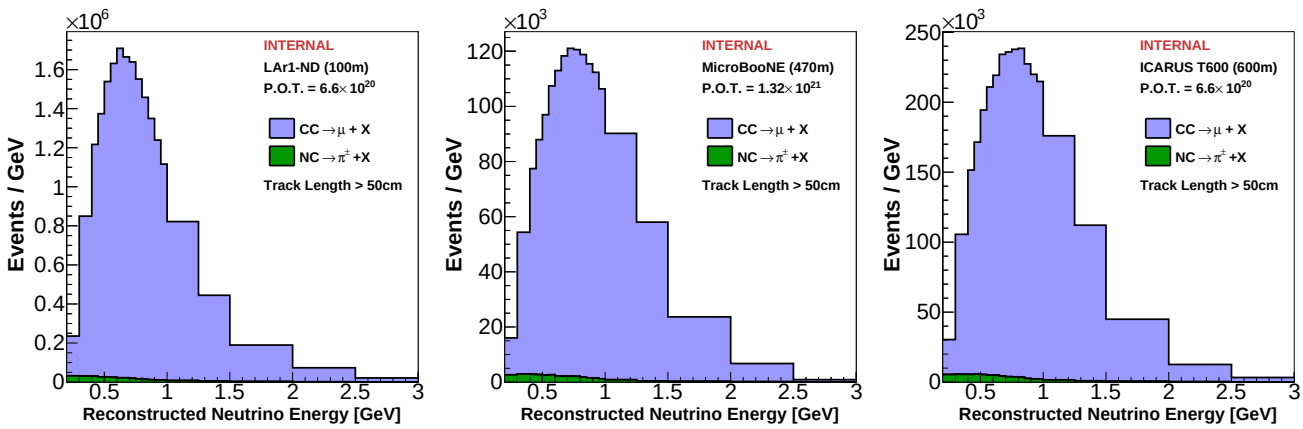

FIG. 12: *Muon neutrino charged-current inclusive events in LAr1-ND (left), MicroBooNE (center), and ICARUS T600 (right). Statistical uncertainties only are shown. Data exposures are indicated on the plots and assume inclusion of the full MicroBooNE data set.*

C. Neutrino Flux Uncertainties

BNB neutrino flux predictions and related systematic uncertainties are assessed using a detailed Monte Carlo program developed by the MiniBooNE Collaboration [3]. In the simulation, charged pion production is constrained using dedicated 8 GeV p+Be hadron production data from the HARP experiment [4] at CERN. Neutral kaon production has been constrained by BNL E910 data [55] and a measurement made at KEK by Abe et al. [56]. K^+ production uncertainties are set by measurements made with the SciBooNE [57] detector when it ran in the BNB. In total, the BNB Monte Carlo treats systematic uncertainties related to the following sources:

- Primary production of π^+, π^-, K^+, K^-, and K^0_L in p+Be collisions at 8 GeV;

- Secondary interactions of p, n, $\pi^{\pm}$ in the beryllium target and aluminum horn;
- Beam focusing with the magnetic horn.

Primary hadron production uncertainties, whenever available, are taken directly from the measured cross sections which are used to constrain the Monte Carlo. In particular, in the case of π^+ and π^- production, the experimental uncertainties reported by the HARP experiment are directly used to set the allowed variation within the beamline simulation.

Secondary interaction uncertainties are also evaluated. Table II summarizes allowed variations on hadron-Be and hadron-Al cross sections in the simulation. The total cross section, σ_{TOT}; the inelastic cross section, σ_{INE}; and the quasi-elastic cross sections, σ_{QEL} are varied separately for nucleons and pions interacting with Be and Al. When we vary σ_{INE} and σ_{QEL} we fix the cross section of the other to hold the total cross section constant.

TABLE II: *Cross section variations for systematic studies of secondary hadron interactions in the target and horn. For each hadron-nucleus cross section type, the momentum-dependent cross section is offset by the amount shown [3].*

	$\Delta\sigma_{\mathrm{TOT}}$ (mb)		$\Delta\sigma_{\mathrm{INE}}$ (mb)		$\Delta\sigma_{\mathrm{QEL}}$ (mb)	
	Be	Al	Be	Al	Be	Al
(p/n)-(Be/Al)	$\pm$ 15.0	$\pm$25.0	$\pm$ 5	$\pm$10	$\pm$ 20	$\pm$45
$\pi^{\pm}$-(Be/Al)	$\pm$ 11.9	$\pm$28.7	$\pm$ 10	$\pm$20	$\pm$ 11.2	$\pm$25.9

Beam focusing systematics include uncertainty on the magnitude of the horn current (174 $\pm$ 1 kA) as well as skin depth effects describing where the current flows on the surfaces of the horn. The skin depth effect allows the magnetic field to penetrate into the interior of the horn conductor which in turn creates a magnetic field within the conductor. This will lead to deflections of charged particles which traverse the conductor, especially higher energy particles which do not penetrate deeply into the horn conductor. The effect can be approximated by modeling an exponentially decreasing field to a depth of about 1.4 mm. To asses the systematic, the field is turned on and off, which leads to an energy dependent effect of 1 to 18% for particles of $<$ 1 GeV to 2 GeV, respectively [3].

We currently don't assess a systematic on hadron interactions with material downstream of the horn (including air, concrete, steel, etc.). These effects have been studied and found to contribute about 1% (2%) to the ν_μ (ν_e) fluxes, so even a large 50% uncertainty would make a negligible contribution to the total errors.

Table II reports the contributions of the underlying systematics to the integrated ν_μ and ν_e fluxes along the BNB, revealing total normalization uncertainties of order 15% on both absolute predictions.

Using Eq. 4 we compute the covariance matrix for all the systematic variations in the flux model. The fractional error matrix and flux correlation matrix are shown in Figure 13. We see that the event rates at different detector locations and for both ν_μ and ν_e fluxes are strongly correlated. These correlations are, of course, the key to SBN sensitivity. The high statistics measurement made in the near detector, together with the high levels of correlations between the near and far locations will eliminate the large normalization uncertainty highlighted in Table II when performing oscillation searches, a critical motivation for the multi-detector SBN configuration.

TABLE III: *Variations in the total flux of each neutrino species in neutrino mode due to the systematic uncertainties [3].*

Source of Uncertainty	ν_μ	ν_e
π^+ production	14.7%	9.3%
π^- production	0.0%	0.0%
K^+ production	0.9%	11.5%
K^0 production	0.0%	2.1%
Horn field	2.2%	0.6%
Nucleon cross sections	2.8%	3.3%
Pion cross sections	1.2%	0.8%

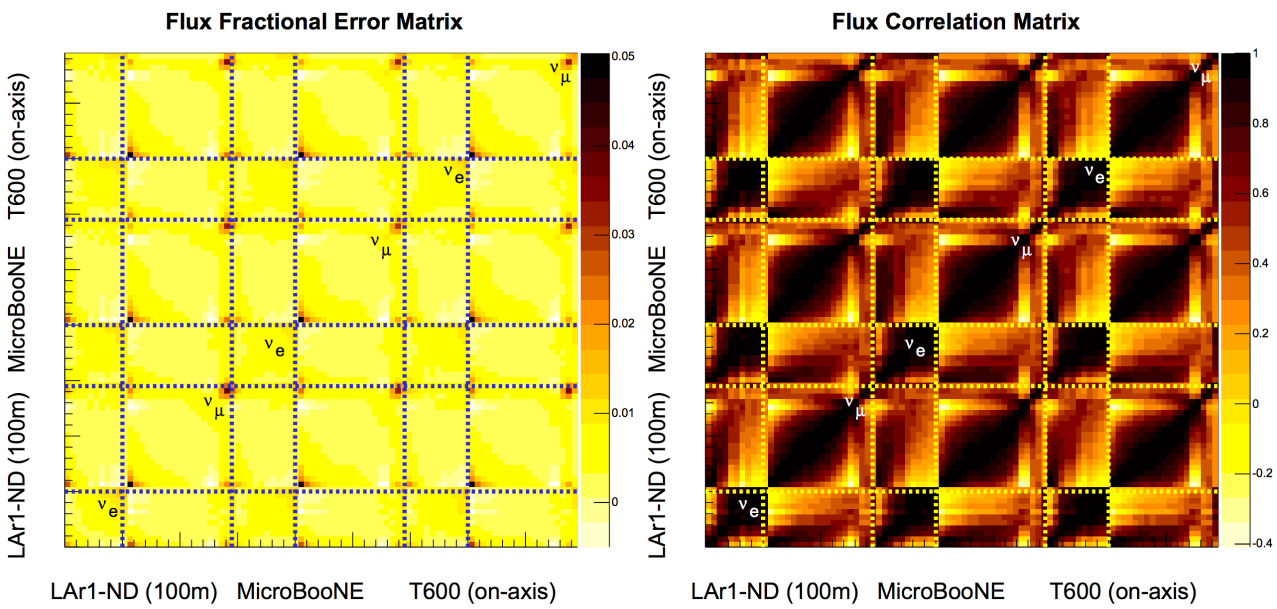

FIG. 13: *The fractional flux covariance matrix (left) and correlation matrix (right). Both the ν_e flux (11 energy bins from 0.2–3 GeV) and ν_μ flux (19 energy bins from 0.2–3 GeV) at all three detector locations are represented; the dashed lines indicate the boundaries in the matrix.*

D. Neutrino Interaction Uncertainties

Uncertainties in the neutrino interaction model[3] are the largest uncertainties affecting the normalization of events in the SBN detectors, but are expected to be highly correlated between detectors because of the use of the same target nucleus (argon). Only through second order impacts of neutrino fluxes or differences in the geometric acceptance of events in the detectors can the correlations be different than +1.0.

Neutrino interaction uncertainties and correlations are evaluated using the GENIE [58] neutrino event generator and the framework of event reweighting that GENIE provides. Table IV lists the uncertainties used for this analysis and their nominal percent variation at 1σ,

[3] including inclusive and exclusive differential cross sections off nucleons, models of the target nuclear medium, and final state interaction effects on produced particles before leaving the nucleus

Parameter	Description	1σ Uncertainty (%)
M_A^{CCQE}	Axial mass for CC quasi-elastic	-15%+25%
M_A^{CCRES}	Axial mass for CC resonance neutrino production	$\pm 20\%$
M_A^{NCRES}	Axial mass for NC resonance neutrino production	$\pm 20\%$
$R_{bkg}^{\nu p,CC1\pi}$	Non-resonance background in $\nu p, CC$ 1π reactions.	$\pm 50\%$
$R_{bkg}^{\nu p,CC2\pi}$	Non-resonance background in $\nu p, CC$ 2π reactions.	$\pm 50\%$
$R_{bkg}^{\nu n,CC1\pi}$	Non-resonance background in $\nu n, CC$ 1π reactions.	$\pm 50\%$
$R_{bkg}^{\nu n,CC2\pi}$	Non-resonance background in $\nu n, CC$ 2π reactions.	$\pm 50\%$
$R_{bkg}^{\nu p,NC1\pi}$	Non-resonance background in $\nu p, NC$ 1π reactions.	$\pm 50\%$
$R_{bkg}^{\nu p,NC2\pi}$	Non-resonance background in $\nu p, NC$ 2π reactions.	$\pm 50\%$
$R_{bkg}^{\nu n,NC1\pi}$	Non-resonance background in $\nu n, NC$ 1π reactions.	$\pm 50\%$
$R_{bkg}^{\nu n,NC2\pi}$	Non-resonance background in $\nu n, NC$ 2π reactions.	$\pm 50\%$
NC	Neutral current normalization	$\pm 25\%$
DIS-NuclMod	DIS, nuclear model	Model switch

TABLE IV: *Neutrino interaction model parameters and uncertainties. This information is reproduced here from the GENIE manual Section 8.1 [58] for convenience.*

according to the GENIE documentation. This is a partial list of the available parameters within the GENIE framework, chosen here for their relevance to the SBN oscillation searches. The analysis does not currently include an estimate of uncertainties on final state interactions.

We simulated 250 different cross section "universes" in which each of the model parameters were varied at random from a Gaussian distribution with a 1σ spread equal to the 1σ uncertainty in the underlying physical quantity. Much more detail is available from the GENIE manual, chapter 8 [59], on both the underlying physical uncertainties and the methodology for propagating them to observed event distributions. Figure 14 shows the RMS of the 250 simulated universes in the reconstructed neutrino energy bins used in the ν_e and ν_μ analyses, indicating absolute neutrino interaction model uncertainties of 10–15%. From these variations, the cross section covariance matrix, $E^{\text{cross section}}$, is constructed using Eq. 4. Figure 14 shows the fractional covariance matrix and correlations for the ν_e charged-current candidate events that were shown in Figure 11. The off-diagonal blocks of the correlation matrix indicate the correlations between events in different detectors. The diagonal elements within the off-diagonal blocks are the correlations between the same energy bins in different detectors and are seen to be near 1.0 in most cases.

E. Detector Systematics

The response of the different detectors has to be known to a sufficient precision to maximize the experimental sensitivity and avoid introducing artificial detector effects mimicking the

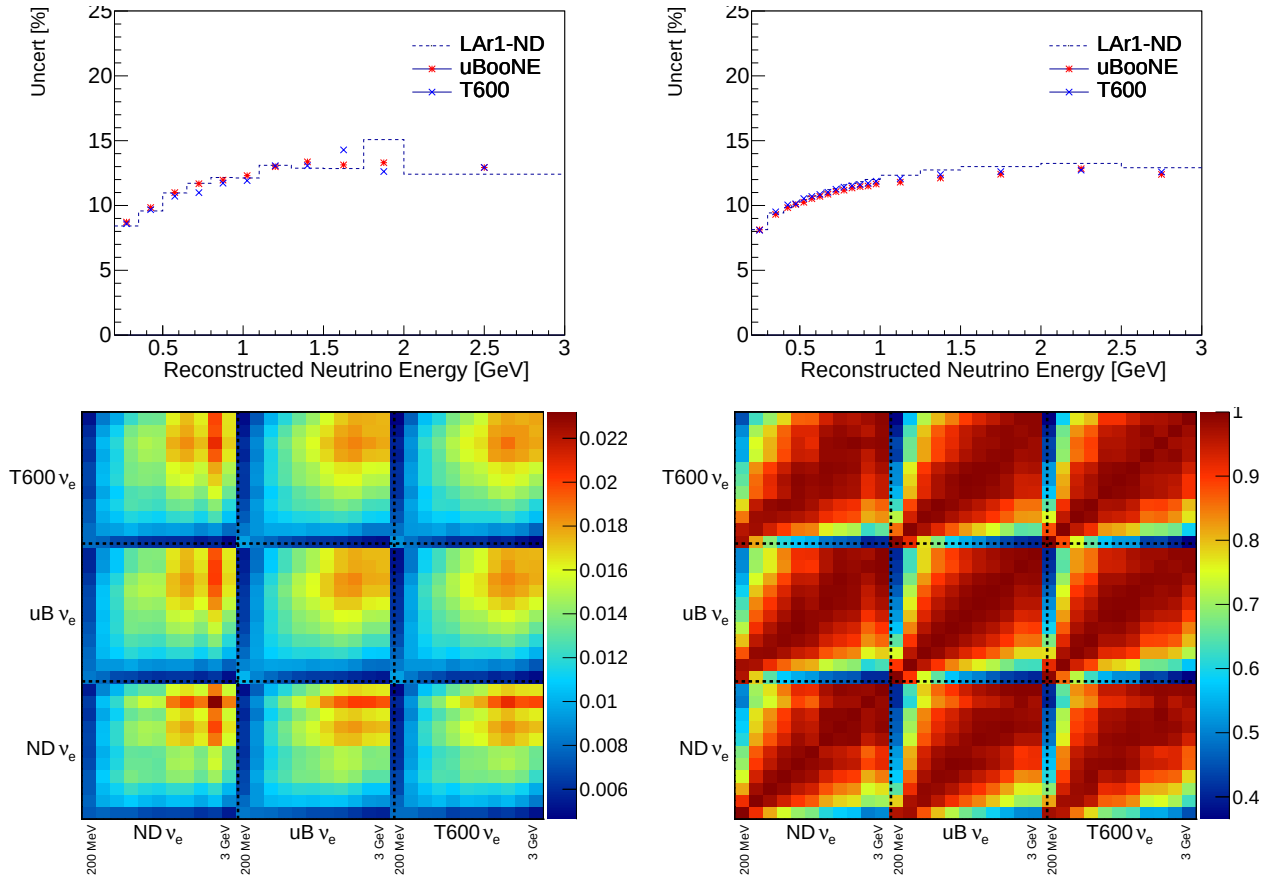

FIG. 14: *Absolute uncertainties on ν_e (upper left) and ν_μ (upper right) event rates at each of the three SBN detectors due to neutrino cross section uncertainties. (Lower left) Fractional cross section covariance matrix, $E^{cross\ section}$, for ν_e CC candidate events. (Lower right) The correlation matrix for ν_e CC candidate events. Inspection of the diagonal elements of the off-diagonal blocks shows the correlations between events in different detectors to be very near 1.0*

sought for oscillation signal. In this respect, the adoption of the same detection technique for all the different detectors and of the same operation conditions, permits to virtually cancel out the impact of the detector response uncertainty on the final measurement.Possible second order effects can arise from differences in the details of the design and implementation of the various detectors. The most relevant physical parameters like the drift field and the TPC structure should be kept as close as possible. Detector systematic effects can be generated by differences between the near and the far detectors, for example:

- The wire orientations in the TPCs;
- TPC readout electronics (shaping, sampling time, S/N ratio, general noise conditions affecting the identification/measurement efficiency);
- Residual differences in the electric drift field (absolute value and homogeneity);
- Residual differences in the detector calibrations including the light collection systems and the identification of off beam interactions by timing;

- LAr purity levels in the detectors;
- Different drift lengths and space charge effects;
- Residual differences in background levels from dirt events and from cosmic rays including different coverage and efficiency of the cosmic tagging systems;
- Effects induced by the different event rates at the two sites, event selection and identification efficiency including the different aspect ratios of the near and far detectors.

As an example, the impact of the different wire orientation on the electron identification efficiency has been studied with a simulation - including the electronic wire signal and noise level actually measured in T600 - of the primary electrons produced in the ν_e CC interactions of the beam. The effect of the different collection wire orientation between LAr1-ND and T600 turns out to be negligible on the expected dE/dx distribution, with $\sim$0.1% variations in the electron identification efficiency on the first 2 cm of the track. The corresponding multiplicity of occupied collection wires is expected to be affected by the different wire orientations and could introduce few percent differences in the electron identification efficiency. This effect would be negligible if the induction wire signals could be exploited too in the dE/dx measurement. Conservatively, measuring dE/dx only with the Collection wire signals and assuming to correct to 20% level with the data themselves the angular dependence of the wire multiplicity, the wire orientation would result in an almost negligible $< 1\%$ systematical effect in the selection efficiency.

It should be noted that all the listed contributions can be directly measured with the data themselves, monitored during the experiment and corrected for in the analysis, largely reducing their impact on the measurement. An overall global detector systematics in the 2–3% range would preserve the experimental sensitivity and the capability to cover at the 5σ level the LSND allowed parameter region. We assume this systematic level as a requirement for the detectors.

F. Beam-Induced "Dirt" Events

Neutrinos from the BNB will interact in material surrounding the active detectors, including liquid argon outside of the TPC, the cryostat steel, structural elements or engineering support equipment in the detector hall, the building walls and floors, and the earth outside the detector enclosure. These interactions can produce photons (through π^0 decay or other channels) which can enter the TPC and convert in the fiducial volume, potentially faking an electron signal. While it turns out the majority of interactions producing this background occur relatively close to the detector volume, the moniker "dirt" events is kept in analogy to its use in MiniBooNE plots and publications. This description, however, will refer to any backgrounds generated by beam neutrino interactions *occurring anywhere outside of the TPC active volume*. We consider this background only for the ν_e analysis as the out-of-detector contamination of the ν_μ charged-current sample is expected to be negligible.

To estimate the dirt background, a Monte Carlo simulation is used which includes a realistic geometry description of the material surrounding the detectors. Due to the large mass but small probability for any given interaction to create energy inside the detector, it is challenging to generate large statistics. Substantial effort was put into generating a large Monte Carlo sample using the MicroBooNE simulation where the geometry description is the most detailed. Figure 15 shows the distribution of interaction vertices for BNB neutrinos which deposit any detectable

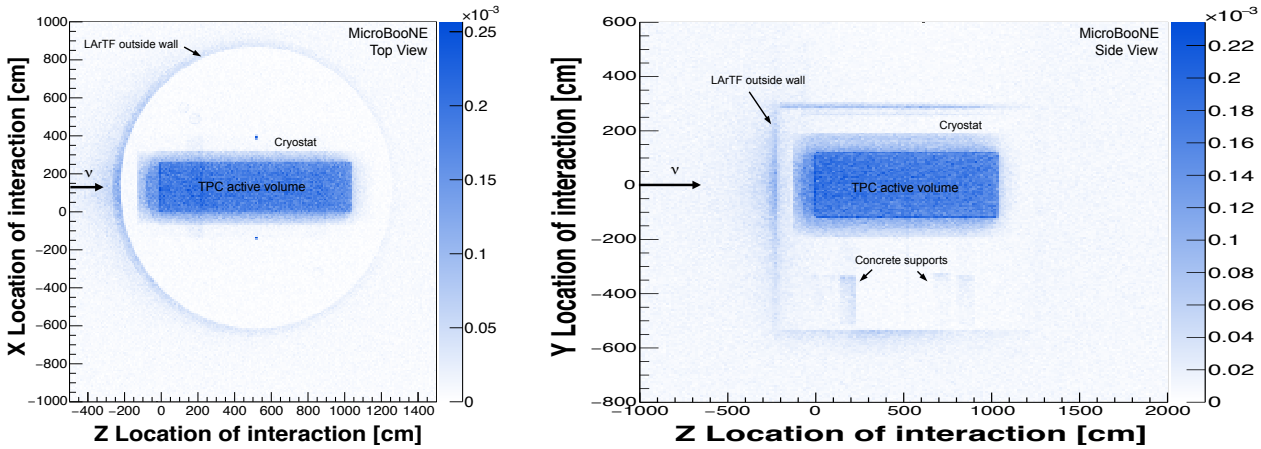

FIG. 15: *Location of interaction vertices for neutrinos which deposit any energy into the MicroBooNE detector shown from above (left) and the side (right).*

energy into the MicroBooNE detector. The walls of the LArTF (Liquid Argon Test Facility) building and the soil surrounding it are clearly visible. In the right image, the concrete supports can be seen, but not the foam insulation saddles that sit between the supports and the cryostat. The highest density of vertices is, of course, in the active volume of the detector.

From this sample, events with an interaction vertex outside of the active TPC volume but that generate a photon which converts inside the detector, are selected. Due to the short radiation length in liquid argon ($X_0 = 14$ cm), the argon volume surrounding the TPC inside the cryostat provides an effective shield for photons trying to enter from beyond the cryostat walls. Most of the interactions capable of creating a photon inside the fiducial volume, therefore, tend to happen in this outer argon region. This can be seen in the upper left panel of Figure 16. The plot shows the creation point of all photons which then convert inside the MicroBooNE active volume, and they clearly pile up in the region just beyond the active volume boundary. Photons entering the detector are likely to interact within a few 10's of centimeters of the TPC boundary, providing a handle with which to minimize this background. The lower panels of Figure 16 show the photon conversion point within the active volume projected onto the z-axis (the beam direction) and the $x - y$ plane. To reduce this background in the ν_e analysis, we restrict the fiducial volume to an inner region of the detector 30 cm from the upstream and 25 cm from the side boundaries of the active TPC region, reducing the number of dirt background events by 80% in MicroBooNE. These fiducial volume boundaries are indicated in the figures for MicroBooNE, but are used uniformly in all three detectors in the analysis.

A similar Monte Carlo sample has been generated for the LAr1-ND detector at 110 m. Figure 17 shows the creation point of all photons which then convert in the LAr1-ND active volume. While the dirt photons in MicroBooNE come in from both the upstream face and the sides of the detector (see Figure 16), in LAr1-ND they are more concentrated at the upstream face of the detector. This difference is due to two factors, *i*) the neutrino flux at the LAr1-ND location is still highly collimated so the event rate is peaked in the middle of the detector and falls off toward the detector sides, while it is uniform across the MicroBooNE detector face, and *ii*) the amount of argon outside of the TPC in the square LAr1-ND cryostat is less than the amount in the cylindrical MicroBooNE cryostat.

A dedicated simulation of out-of-detector interactions at the ICARUS T600 site has not been generated. Instead, because the 470 m and 600 m locations are both in the region where

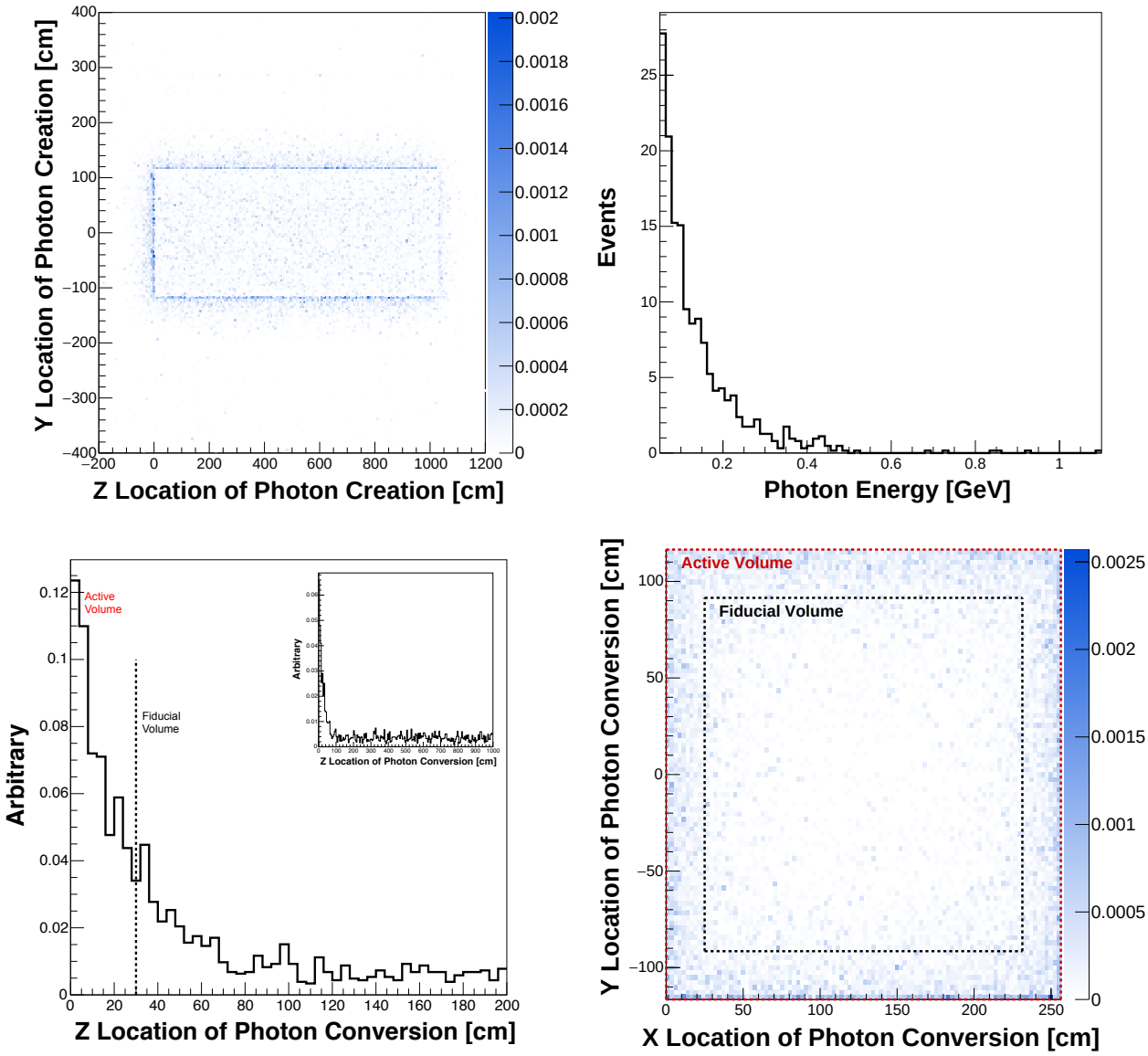

FIG. 16: *(Top left) Photon creation position in the Y–Z, side view, projection for photons which then convert inside the MicroBooNE active volume, possibly faking a ν_e CC interaction. (Top right) Energy of the photons that convert inside the MicroBooNE detector but came from neutrino interactions outside of the detector active volume. (Bottom left) Photon conversion position inside the MicroBooNE detector projected onto the z-axis ($z = 0$ is the start of the TPC active volume; only first 200 cm shown). The vertical dashed line is 30 cm from the front of the TPC. (Bottom right) Photon conversion position in the X-Y, front view, for photons which convert downstream of $z = 30$ cm (plot boundary is the TPC active volume; fiducial volume for ν_e analysis is indicated).*

the flux is wider than the detectors, we can use the MicroBooNE predictions to scale to the far detector site and generate an estimate of the dirt background in ICARUS. We account for the different surface areas of the two detectors and scale the neutrino flux as $1/r^2$. To account for any differences in the background rate from photons entering the front vs. the sides of the detectors, we scale events in the beginning 50 cm of the MicroBooNE detector separately from

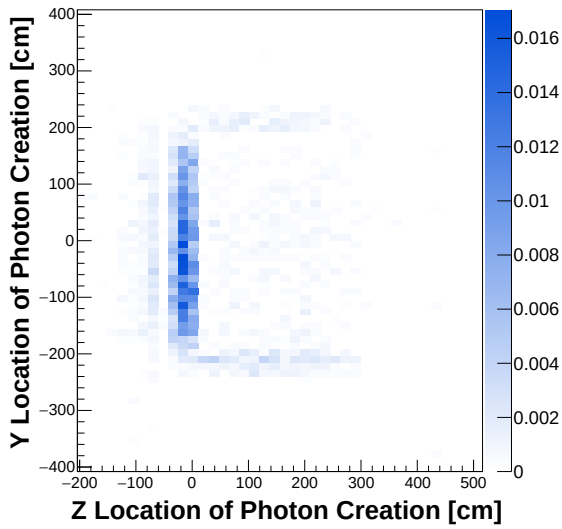

FIG. 17: *Photon creation position in the Y–Z, side view, projection for photons which then convert inside the LAr1-ND active volume.*

those further downstream:

$$N_{\text{dirt}}^{\text{T600}} = \frac{470^2}{600^2} \times 2 \times \left(\frac{\text{Front Area T300}}{\text{Front Area } \mu\text{BooNE}} N_{\text{dirt}}^{\mu B}(z \leq 50 \text{ cm}) + \frac{\text{Side Area T300}}{\text{Side Area } \mu\text{BooNE}} N_{\text{dirt}}^{\mu B}(z > 50 \text{ cm}) \right) \quad (7)$$

where $N_{\text{dirt}}^{\mu B}(z)$ is the number of dirt events predicted in MicroBooNE and z is the distance from the front of the active volume. Table V provides the total number of dirt background events expected in each detector according to the simulations for LAr1-ND and MicroBooNE and using Eq. 7 to estimate the rate in ICARUS.

TABLE V: *Estimated background levels in the ν_e charged-current sample from out-of-detector neutrino interactions in a 6.6×10^{20} POT exposure.*

Detector	Estimated Dirt Background Events (6.6×10^{20} POT)		
	$z \leq 50$ *cm*	$z > 50$ *cm*	Total
LAr1-ND	26.2	17.0	43.2
MicroBooNE	2.38	19.5	21.9
ICARUS T600	5.15	57.0	62.2

Finally, we require an estimate of the error matrix associated with dirt backgrounds, E^{dirt}. The dirt background rate in each detector can be constrained with data using a sample of electromagnetic shower events near the TPC boundary, or showers where the reconstructed momentum is consistent with the particle having entered the detector. This sample will be enhanced in dirt background events and can be used to validate the simulations. At this time, we conservatively estimate a 15% systematic uncertainty uncorrelated between detectors, but fully correlated within the energy spectrum in each detector. This covariance matrix is

constructed as

$$E_{ij}^{\mathrm{dirt}} = (0.15 \times N_i^{\mathrm{dirt}})(0.15 \times N_j^{\mathrm{dirt}}) \tag{8}$$

within each detector and is included in the sensitivity calculations.

In the present analysis, we reduce the dirt background to manageable levels by restricting the fiducial volume used in the ν_e analysis. A more sophisticated approach has also been explored that would use the reconstructed shower direction in candidate events to project *backwards* from the vertex and calculate the distance to the nearest TPC boundary in the backwards direction. Cutting on this quantity on an event-by-event basis would allow us to further reduce the dirt backgrounds on all sides without sacrificing fiducial volume. This is referred to as the *backwards-distance-to-wall* variable, and is not used in the current analysis.

G. Cosmogenic Backgrounds

Another important background to the ν_e analysis is created by cosmogenic photons that generate electrons in the detector via Compton scattering or pair production interactions that are misidentified as a single electron. Photons are created either in the atmospheric shower ("primary photons") or by cosmic muons propagating through the detector and nearby surrounding materials ("secondary photons"). In the case of an un-shielded detector at the surface, the background to a ν_e CC sample is mostly due to primary photons, but these can be easily absorbed by a few meters of earth or concrete shielding. In simulations of the far detector, for example, a 3 m rock coverage reduces by a factor 400 the number of primary photons above 200 MeV in the active volume, and secondary photons generated by muons passing through or very near the detectors becomes the dominant source of background. To further reduce the rate, we must identify cosmic showers through topological and timing information in the event.

In an ideal situation where precise timing information is known for every track or shower inside the detector, only cosmogenic events in coincidence with the beam spill can contribute to the background. However, in a realistic situation, interactions occurring anytime within the acquisition time (which corresponds to the maximum electron drift time) may influence the data analysis, as will be explained below. Given the respective detector sizes, the maximum drift times are 1.28 ms in LAr1-ND, 1.6 ms in MicroBooNE and 0.96 ms in ICARUS, to be compared with the 1.6 μs duration of the beam spill from the BNB. Potential cosmogenic backgrounds can be categorized according to their time structure as:

Timing case A: Cosmogenic photon interacts in the detector in coincidence with the beam spill.

Timing case B: Cosmogenic photon interacts anywhere inside the drift time, and a *different* cosmic event (muon or otherwise) is in the detector in coincidence with the beam spill. If the arrival time of the photon is poorly known, it could be mistaken for the in-spill event.

If not properly recognized, neutrino beam interactions occurring in LAr surrounding the TPC active volume or low energy neutral-current interactions that are not identified, can also provide a scintillation trigger in the beam spill leading to a situation similar to timing case B. Due to the relatively low neutrino interaction rate, this effect is smaller and is not currently included in the analysis, but has been roughly estimated in the illustration for the far detector in Table VIII.

Key topological information includes the location of the photon within the detector (just as with dirt events, externally produced γs will interact near the detector edges) and the proximity to the parent cosmic muon track in the case of secondary photons. Therefore, we identify two main categories of event topology:

Topology I: Cosmogenic photon interacts inside the fiducial volume, and the parent muon also enters the TPC active volume.

Topology II: Cosmogenic photon interacts inside the fiducial volume, but the photon originated from the atmospheric shower (a primary), the parent particle is not visible (e.g. neutrons), or the parent particle does not enter the TPC active volume (e.g. muon misses the active volume).

It should be emphasized that the most important outcome at this time is to understand if cosmogenic backgrounds can be reduced to a level that oscillation signals will be observed with sufficient $S/\sqrt{B}$. The absolute rate of events in the experiment will not introduce significant *systematic* uncertainty because it will be measured with high precision using off-beam random event triggers. This is a critical aspect of the experiment, and designing the DAQ systems to record sufficient random triggers must be considered.

Estimation of the cosmogenic background rate requires a detailed simulation of the cosmic particle fluxes and their interactions in and around the detectors. As with the dirt backgrounds described in Section II F, a realistic geometry description and significant computational effort is required. For the current analysis, independent simulations have been developed by the MicroBooNE, LAr1-ND, and ICARUS collaborations. All future analysis of SBN data will, of course, be based on a common simulation, but the current development has provided some important opportunities for cross checks. We provide here brief descriptions of each simulation:

- ICARUS: The ICARUS simulation uses FLUKA [52, 53] for both the cosmic ray showering and the particle transport to and inside the detector. FLUKA is a multipurpose Monte Carlo code used for several years to simulate cosmic showers in the atmosphere. Examples of its performance can be found in the literature, for instance the simulated flux of muons at different depths in the atmosphere agrees with CAPRICE data within experimental errors [60]. Similar agreement [61] is obtained with the muon spectra measured by the L3 experiment, and predicted proton and lepton fluxes in the atmosphere are in very good agreement [62] with the AMS data. The ICARUS simulation is the most complete in that it includes both proton and ion primary cosmic ray sources and generates all particle content in the showers. Primary neutrons, for example, are found to contribute about 10% of electron-like events. The energy spectra of different particle types predicted by the FLUKA simulations at 260 m above sea level (FNAL elevation is 225 m) are shown in Figure 18. The detector was simulated at the surface (not in a building) with and without 3 m of concrete overburden above the detector as mentioned above. The default in this analysis is *with* overburden.

- MicroBooNE: The MicroBooNE simulations are performed with the CRY cosmic-ray shower simulation [63] as a primary particle generator and GEANT4 to transport particles into the MicroBooNE detector. The CRY package provides reasonable results in a fast and easy way, but has known limitations, such as the lack of a contribution from primary ions, a rigid binning structure that sacrifices some spectral details, and an under prediction of neutron, proton, electron, and γ shower content. Comparisons have shown that results

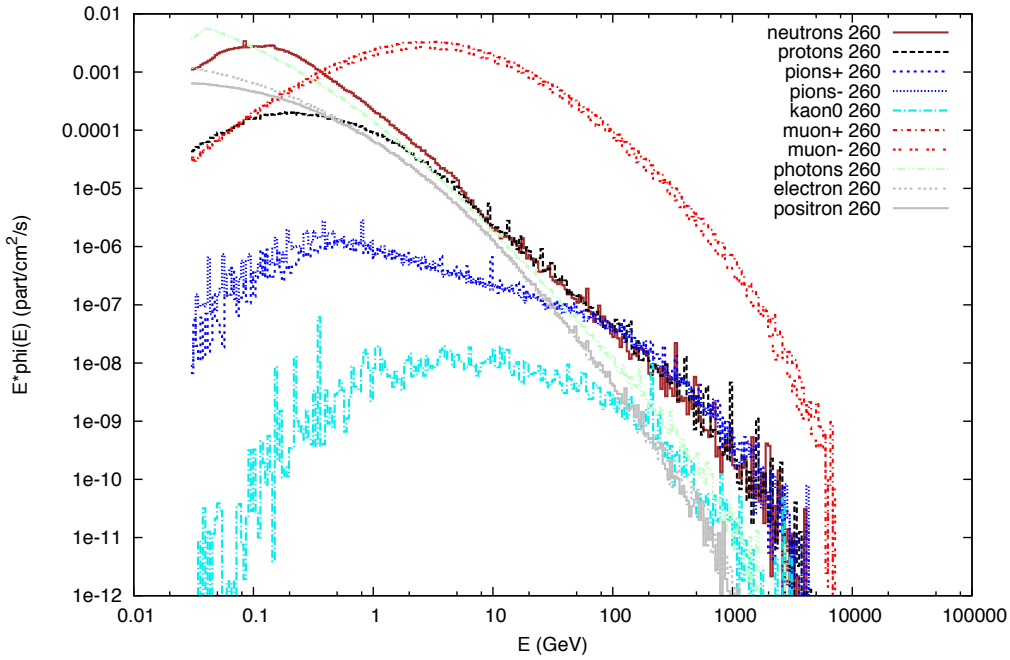

FIG. 18: *(Left) Particle fluxes in the atmosphere at 260 m elevation (FNAL is at 225 m) according to the FLUKA simulation.*

obtained with CRY+GEANT4 in MicroBooNE and results scaled from the full FLUKA T600 simulation agree within a factor of two. The detector geometry is the most detailed and includes the LArTF building and substantial infrastructure, so there is some shielding effects from the building and platforms above the detector. The LArTF facility also has the ability to support concrete shielding blocks on the roof, but this is *not* included in the present simulations. Studies are continuing by the MicroBooNE collaboration to determine if the additional shielding should be added for the upcoming physics run.

- LAr1-ND: The LAr1-ND cosmic muon flux is generated using Gaisser's parameterization [64], with corrections for the Earth's curvature and the muon lifetime. The muon flux simulation is performed at the Fermilab latitude, and muons are propagated through the LAr1-ND detector and building using GEANT4. The detector is simulated in a pit below grade, but without shielding above the detector. Only the muon component of the shower is included, but results from both the ICARUS and MicroBooNE simulations show this is by far the dominant contribution to the background, and the exclusion of primary photons and hadrons in the simulation is nearly equivalent to simulating a detector with some overburden.

To get a sense for the situation, it is instructive to first look at some basic numbers coming from the far detector simulation. Cosmogenic interactions of all kinds depositing more than 100 MeV of energy will occur in the T600 fiducial volume at ∼11 kHz, implying such an event inside the detector during 1 out of every 50 beam spills. A 6.6×10^{20} POT run represents approximately 1.32×10^{8} spills at nominal intensity, corresponding to 211 seconds of beam-on time throughout the experiment. ICARUS will, therefore, see 2.5×10^{6} cosmic events *during the beam spill time* in the run. Further, ∼10 cosmic muon tracks will enter into the detector volume during the 0.96 ms drift time in each readout of the detector.

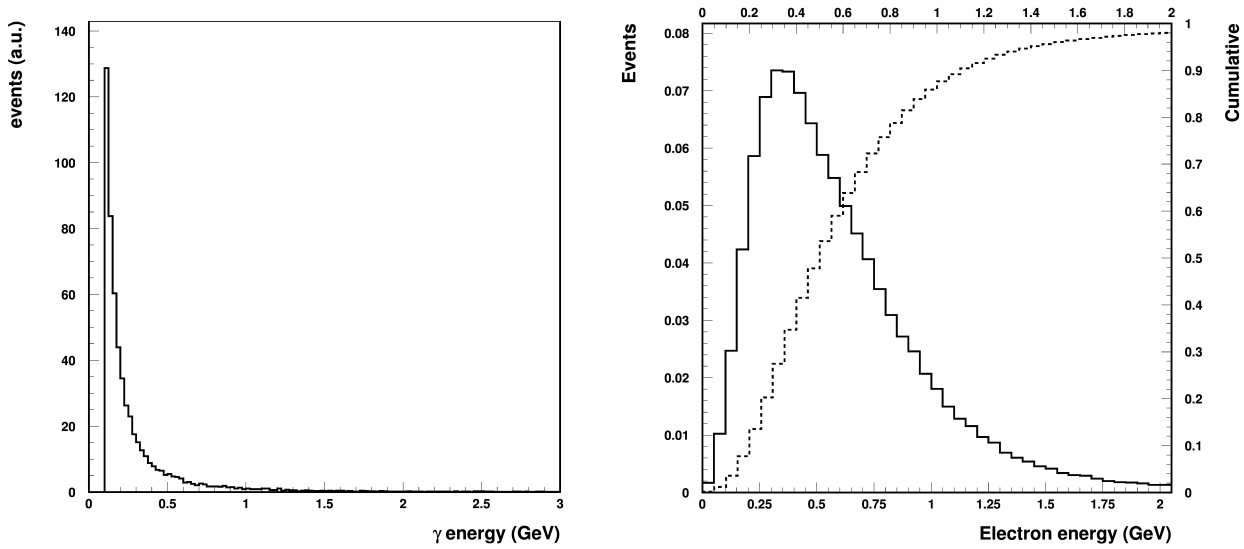

FIG. 19: *(Left) Energy distribution (in GeV) of cosmic background photons inside the far detector. (Right) Energy distribution of electrons produced in ν_e interactions in the far detector.*

Figure 19 (left) shows the energy distribution of cosmogenic photons which interact in the TPC fiducial volume as calculated by far detector simulation (the others look similar, of course). The spectrum is steeply decreasing with energy. For reference, Figure 19 (right) shows the photon total cross section in argon in this energy range and the contributions of pair production (off a nuclear or electron field) and incoherent scattering (Compton scattering off an electron) [65].

Cosmogenic photon interaction rates have been estimated in the three detectors using the simulations described above and the results are detailed in Table VI. In each detector, fiducial cuts as suggested by the beam dirt events analysis (Section II F) have been applied, namely 25 cm from the sides of the active volume, 30 cm from the upstream face, 50 cm from the downstream face, and 1.5 cm from the cathode when applicable. Rates for both topology I and II events occurring within the beam spill (timing category A) are estimated directly from the simulations by scaling the time exposure represented in each Monte Carlo sample to 211 seconds. Rows 1–4 of Table VI give the raw rates for both Compton and pair producing photons inside the fiducial volume with and without a parent muon that enters the TPC active volume. These numbers reveal several interesting features. First, the ratio of row 1 to row 2 is $\sim$2% in each case, which is consistent with the size of the Compton scattering cross section in this energy range. Second, a comparison of rows 3–4 to 1–2 indicates that the liklehood of a photon converting in the fiducial volume where the parent muon completely misses the TPC is very small. The 25 cm active buffer around the fiducial volume motivated by the dirt backgrounds is also very effective at absorbing cosmogenic photons entering the detector from outside. And as we will describe below, the presence of the parent muon in the TPC provides a strong handle for rejecting the photon shower as a beam-related event. Finally, comparing the different columns of rows 1–4 does reveal some variability in the predicted cosmic photon rates in the three detectors. Factors of 2-3 may be expected due to differences in the input simulations as described above. The geometry of the detectors plays a role in the expected

TABLE VI: *Background rates, assuming 3 years of data taking for a total of* 6.6×10^{20} *protons on target, delivered in* 1.32×10^8 *beam spills equaling 211 seconds of beam time. Events with at least one photon shower above 200 MeV converting in the fiducial volume are counted in all the* γ *entries.*

	Cosmic photon interaction description	Timing Cat.	Topology Cat.	$E_\gamma > 200$ MeV, Pair prod $E_e > 200$ MeV, Compton LAr1-ND	μBooNE	ICARUS
1	γ Compton in spill, primary μ enters AV	A	I	887	206	599
2	γ Pair prod in spill, primary μ enters AV	A	I	52,300	11,600	32,000
3	γ Compton in spill, primary misses AV	A	II	<1	<3	<4
4	γ Pair prod in spill, primary misses AV	A	II	55	82	11
5	γ Compton in drift, primary μ enters AV	B	I	2,250	1,030	3,300
6	γ Pair prod in drift, primary μ enters AV	B	I	132,900	57,950	176,000
7	γ Compton in drift, primary misses AV	B	II	<3	12.4	<4
8	γ Pair prod in drift, primary misses AV	B	II	140	410	60

rates, as well. For example, the probability that a crossing muon produces a photon in the detector will scale as the average muon track length in the detector, and LAr1-ND has the largest average track length due to the detector's 4 m height.

Rows 5–8 of Table VI present the number of events of timing category B and are calculated directly from rows 1–4. We assume, to first order, that the time signal during the beam spill is produced by a cosmic muon entering the detector. Event category B is reducible if light signals in the argon are able to be correctly matched to the energy deposits that produce them, however, we initially assume this is not done. The number of category B events can then be calculated from the number of category A events that were estimated directly from the simulation. The scale factor ends up being N_μ^{drift}, the average number of muons that enter the detector per readout during the full drift time:

$$N_B = P_\gamma^{\text{drift}} \times P_\mu^{\text{spill}} = \left(N_A * \frac{t_{\text{drift}}}{t_{\text{spill}}} \right) \times \left(N_\mu^{\text{drift}} * \frac{t_{\text{spill}}}{t_{\text{drift}}} \right) = N_A * N_\mu^{\text{drift}} \tag{9}$$

Our simulations indicate that $N_\mu^{\text{drift-LAr1-ND}} = 2.5$, $N_\mu^{\text{drift-MicroBooNE}} = 5.0$, and $N_\mu^{\text{drift-T300}} = 5.5$. The T300 is the right unit for the ICARUS detector since each T300 module is an optically isolated element of the full T600 detector.

Table VI represents the raw number of cosmogenic photons that interact within the fiducial volumes of each detector during the proposed run. A number of strategies can be applied to reduce the cosmic backgrounds entering the ν_e analysis sample. Below we list the strategies being considered. Items 1–5 describe topology based cuts using TPC information only. Items 6–8 use precise timing information to reject events that are not coincident with the neutrino beam or to eliminate TPC beam triggers that are contaminated by cosmic activity in the detector during the beam spill.

1) dE/dx: Pair production events can be rejected with the reconstruction of dE/dx in the initial part of the shower. Preliminary results show that only 6% of pair conversions present a dE/dx lower than 3.5 MeV/cm in the first 2.5 cm of the shower.

2) Distance from the muon track: Figure 20 shows the distance of the cosmogenic photon conversion point from the parent muon track, whenever it also crosses the detector. A

cylindrical "muon anti-fiducial volume" of 15 cm radius around each muon track cuts >99% of the background photons above 200 MeV. The resulting loss in fiducial volume for the ν_e analysis ($\sum_\mu \pi R^2 L_\mu$) is minimal, ∼1% per event on average in the far detector considering all muons in one drift time in one module.

3) Clustering around muon tracks: Rather than a fixed cylindrical volume around tracks as in strategy 2), a variable "anti-fiducial" cut around each muon/charged particle can be defined by the zone of connected electromagnetic activity. The "connection" is built by walking out from the primary track, clustering hits and gathering clusters together. This appears to be a very effective cut, however its stability in different wire orientations and noise conditions has to be further established.

4) Activity at the vertex: Requiring the presence of another ionizing track from the vertex would reject all Compton events and a further fraction of the pair production events. However, the same selection on ν_e events discards ∼25% of the signal, making this a cut of last resort.

5) Backwards distance to the detector wall: This cut was introduced above in our discussion of dirt backgrounds to more efficiently identify showers from photons generated outside of the detector. Using the reconstructed shower direction in candidate events, one can project back from the vertex and calculate the distance to the nearest TPC boundary in the backward direction. Since the cosmogenic background is dominated by photons generated by muons inside the active volume, this cut has limited impact and needs further investigation before being applied.

6) Scintillation light: Precise event timing information is available through the detection of scintillation light in the liquid argon. If PMT signals can be matched to the corresponding ionization signals with high efficiency, this would allow a large reduction of backgrounds falling into the timing category B introduced above. Studies are ongoing to characterize the matching performance and optimize the light collection systems in both LAr1-ND and ICARUS.

7) Proton beam spill time structure: Measurement of event times with ∼1-2 ns accuracy would enable the exploitation of the bunched beam structure within the spill (∼2 ns wide bunches every 19 ns, see Section I A), to reduce cosmic backgrounds a factor of 3-4 by rejecting events that occur between bunches. The possibility to reduce the number of bunches by a factor of 2-3, while keeping the same number of protons per spill, will also be investigated in order to further increase this rejection factor.

8) Muon tagging: A powerful way to reduce cosmogenic backgrounds would be to employ a cosmic tagging system external to the TPC volume capable of independently measuring the position and time of entering charged tracks. This information would greatly facilitate the reconstruction and identification of muon tracks in the TPC, leading to a reduction of both type A and B background categories. In the simplest application of this information, an external tagging and tracking system with high (e.g. >95%) coverage of the muon flux that creates potential backgrounds could be used to identify and reject detector readouts when a cosmic μ passes near the detector during the proton beam spill. Expected fluxes at the detector locations indicate this would reduce the beam data sets by roughly 2.5%, 3%, and 5% at LAr1-ND, MicroBooNE, and ICARUS, respectively, while reducing the cosmic backgrounds in a very clean way.

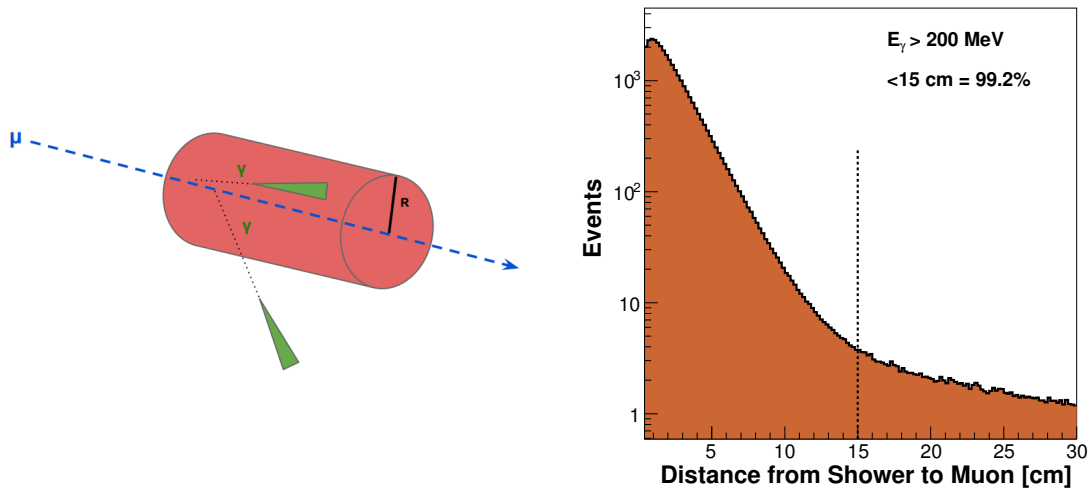

FIG. 20: *Shortest distance between the conversion point of cosmogenic photons and the parent muon track for photons above 200 MeV.*

Table VII illustrates the performance of topological cuts 1) and 2) applied to the Monte Carlo simulations. In particular, photon showers within 15 cm of the muon path are rejected and 94% of γ pair production showers are rejected corresponding to a $dE/dx > 3.5$ MeV/cm cut on the first 2.5 cm of the shower. Remaining background levels in the three detectors (order 100 events) are summarized in Table VII, which can be directly compared to Table VI before these cuts. Also, listed for comparison are the expected numbers of intrinsic ν_e CC events and an example ν_e signal corresponding to the best fit oscillation parameters from [33]. In Section II H, we will present predicted event distributions when using these topological cuts, as well as illustrate the power of augmenting these with external muon tagging and timing selections.

TABLE VII: *Background rates, after topological cuts, assuming 3 years of data taking for a total of* 6.6×10^{20} *protons on target, delivered in* 1.32×10^8 *beam spills equaling 211 seconds of beam time. The cuts that have been applied relative to Table VI are (distance from the* μ *track)* < 15 *cm and* $dE/dx > 3.5$ *MeV/cm.*

	Interaction description	Timing Cat.	Topology Cat.	$E_\gamma > 200$ MeV, Pair prod $E_e > 200$ MeV, Compton, ν_e LAr1-ND	μBooNE	ICARUS
1	γ Compton in spill, primary μ enters AV	A	I	8	<3	<4
2	γ Pair prod in spill, primary μ enters AV	A	I	26	6	21
3	γ Compton in spill, primary misses AV	A	II	<1	<3	<4
4	γ Pair prod in spill, primary misses AV	A	II	<4	6	<1
5	γ Compton in drift, primary μ enters AV	B	I	20	12	30
6	γ Pair prod in drift, primary μ enters AV	B	I	66	29	113
7	γ Compton in drift, primary misses AV	B	II	<3	12	<4
8	γ Pair prod in drift, primary misses AV	B	II	8	19	<4
	Total Cosmogenic γ backgrounds			134	88	164
	Intrinsic ν_e CC			15,800	413	1,500
	Signal ν_e CC ($\Delta m^2 = 0.43$ eV^2, $\sin^2 2\theta = 0.013$)			140	84	615

An Illustration of Cosmogenic Rate Reductions in ICARUS

As an illustration of the detector capabilities in rejecting the cosmogenic background, the external muon tagging system and event matching to the proton spill time structure (introduced in [66], [67]) can be applied in the first stages of the data selection in order to achieve an effective reduction of the data amount to be fully analyzed (Table VIII).

TABLE VIII: *Expected background event reduction in the T600 detector exploiting the muon tagging system and the beam spill time structure. Event topology I refers to events with a muon track crossing the active TPC volume and Event Topology II refers to events with no visible muon in the TPC. The contribution from the non-identified neutrino interactions is also added.*

	Cosmic Background Events	
Total cosmic events in beam spills (211 sec. total)	2.5×10^6	
Cosmic triggers after the tagging system	2.4×10^4	
Surviving events after the spill structure exploitation	8020	
	Event Topology	
	I	II
γ conversions	600	3
After distance from muon cut (15 cm)	6	3
Remaining cosmogenic backgrounds after dE/dx cut	1	
Remaining cosmogenic background in non-identified BNB ν interactions	18	
Total cosmogenic background after scintillation light exploitation	5	

From the previous calculations of the cosmic ray flux impinging on the T600 detector (see Table VI), the predicted number of triggers produced by cosmics inside the 1.6 μs beam spill is globally $\sim 2.5 \times 10^6$ events. The corresponding predicted fraction of γ-ray conversions per imaging picture is about 0.12.

The external muon tagging system can directly reduce the number of triggers produced by cosmic rays to $\sim 2.4 \times 10^4$ events, mostly associated with the $\sim 15\%$ fraction of muons stopping inside the detector, assuming a 95% detection efficiency at each crossing. Assuming a factor 3 of reduction can be achieved from the exploitation of the beam spill time structure, a total of ~ 600 events with a converting γ with $E > 200$ MeV associated to a muon crossing the active TPC volume (event topology I) are expected in the T600. As described above, only 1% of converting γ's accompanied by a visible muon will satisfy the requirement of a minimal distance of 15 cm of the photon conversion from the muons, leaving ~ 6 events.

In addition, from Table VI, γ-ray conversion ($E > 200$ MeV) events are expected without a visible muon in the TPC's (event topology II) in time with the bunched beam structure and under the conservative assumption that only 50% of them is recognized by the tagging system. Therefore the surviving 9 event sample is further reduced to ~ 1 events by the reconstruction of the dE/dx in the initial part of the shower.

If not properly recognized, neutrino beam interactions at low energy occurring both in active volume and in the external LAr could mimic a cosmogenic trigger in time with the beam spill. In such a case cosmogenic photons inside the drift time are expected to contribute to the background escaping any mitigation effect from the muon tagging system and the precise time matching with the beam spill structure. A rough conservative estimation of $\sim 3 \times 10^5$ events

will result in 18 events satisfying the previous selection criteria, namely the requirement of the minimal 15 cm distance from muon and dE/dx identification.

The resulting total ~ 19 background events could be further reduced to ~ 5 events under the conservative assumption that the scintillation light system is capable to localize the triggering event within ~ 4 m along the beam direction.

The explicit request of absence of muon tagging in the event and the precise time matching with the bunched spill structure are expected to slightly reduce the ν_e CC event acceptance by $\sim 3\%$. The 200 MeV electron energy threshold will result in a reduction of $\sim 10\%$ on the electron signal acceptance, while the corresponding reduction for a request of a minimal distance of the event vertex from the cosmic muon tracks is almost negligible, 0.7% on average.

H. $\nu_\mu \to \nu_e$ Appearance Sensitivity

We are now ready to bring together the background predictions and uncertainty estimations detailed in the previous Sections to construct the experimental sensitivity to $\nu_\mu \to \nu_e$ oscillations. Figure 21 shows the full ν_e background predictions in each detector, including intrinsic ν_e beam events, neutral-current and ν_μ CC mis-IDs, out-of-detector beam related "dirt" backgrounds, and cosmogenic photon induced electromagnetic shower backgrounds. For comparison, a sample $\nu_\mu \to \nu_e$ oscillation signal is also included at each detector location corresponding to the best-fit parameters from the Kopp et al. analysis [33] of $\Delta m^2_{41} = 0.43$ eV^2 and $\sin^2 2\theta = 0.013$.

On the left in Figure 21 is shown the result when using the topological cuts 1) and 2) described in Section II G to reduce cosmic backgrounds. This analysis, using dE/dx information and the 15 cm cylinder cut around crossing muons, demonstrates the power of TPC information alone in reducing these backgrounds, rejecting more than 99% of cosmogenic photons when their parent muon is also visible in the TPC. However, as can be seen in the figures, the cosmogenic backgrounds remain a large contribution to the analysis, particularly at low energies, and additional hardware-based systems that can initially reduce the data sample in a very clean way are considered important additions to guarantee the success of the experiment.

The right column of Figure 21 demonstrates the potential improvement when employing additional hardware solutions such as those introduced in Section II G. Precise timing information, in particular, can augment the TPC data by rejecting triggers where the 1.6 μs beam spill time is contaminated by a cosmic event in the detector. To generate the right hand distributions of Figure 22, it is assumed that the combination of strategies 6–8 from above are applied to remove 95% of cosmogenic events in the first stages of data analysis, before entering into automated reconstruction and event selection algorithms. Given the dominance of muons passing very near the detectors as the source of cosmic backgrounds, most of this reduction should be straightforwardly achievable with a properly implemented external tracking system. Further rejection capabilities will come from precise event timing information from internal scintillation light collection systems, making this factor of 20 reduction a fairly conservative estimate of the power of strategies 6–8 combined.

Table IX lists the integrated event totals represented in the histograms of Figure 21. The 20$\times$ reduction from additional cosmic tagging discussed above is indicated in parenthesis. Vetoing of events with cosmic activity in the beam spill using timing results in a reduction of all beam related event categories of 2.5%, 3%, and 5% in LAr1-ND, MicroBooNE, and ICARUS, respectively, which is not shown in the Table (for clarity) but is accounted for in Figure 21 (right) and in the final sensitivity. One thing to note in Table IX is that the event counts

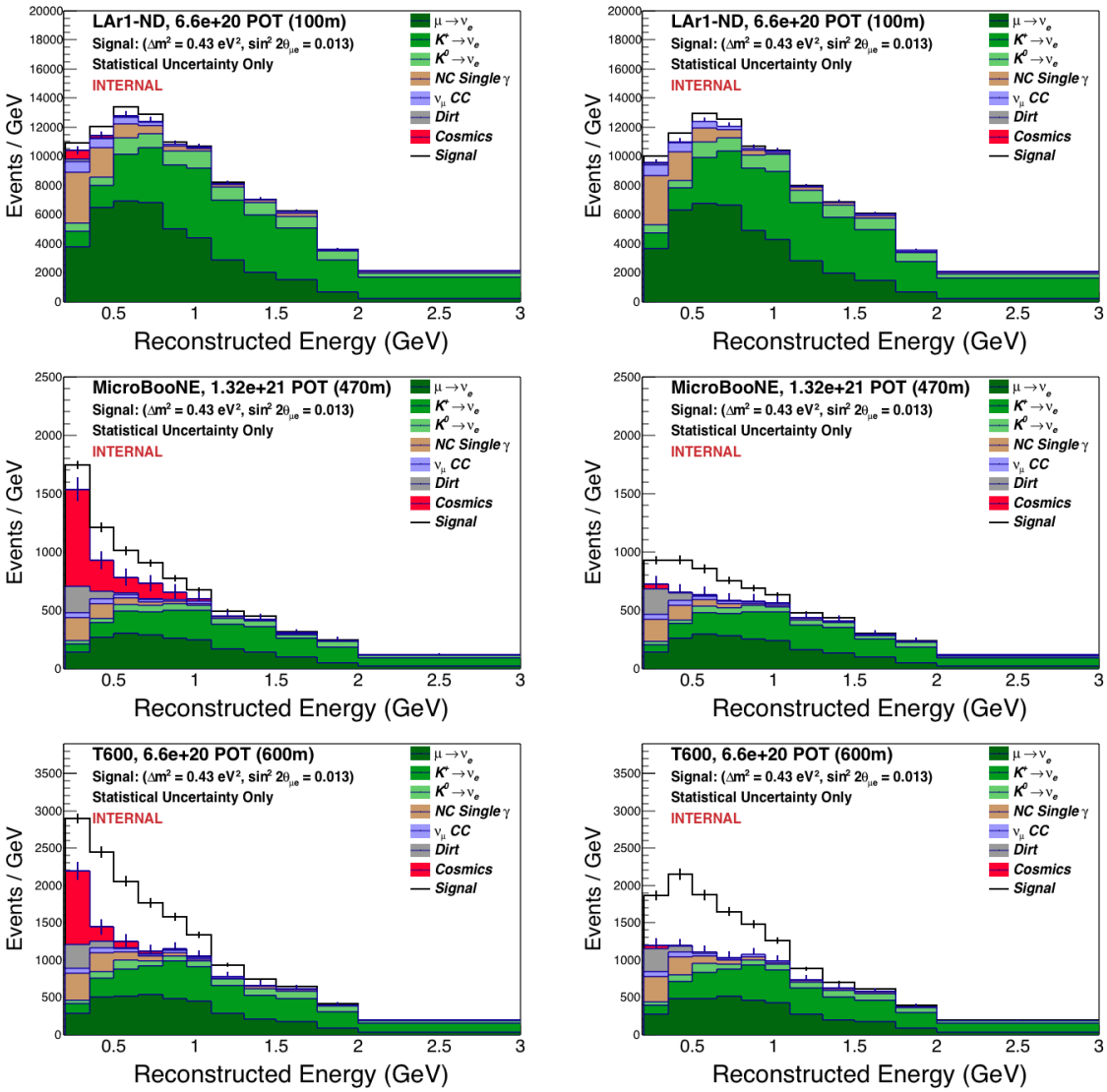

FIG. 21: *Electron neutrino charged-current candidate distributions in LAr1-ND (top), MicroBooNE (middle), and ICARUS T600 (bottom) shown as a function of reconstructed neutrino energy. All backgrounds are shown. In the left column, only muon proximity and dE/dx cuts have been used to reject cosmogenic background sources. In the right column, a combination of the internal light collection systems and external cosmic tagger systems at each detector are assumed to conservatively identify 95% of the triggers with a cosmic muon in the beam spill time and those events are rejected. Oscillation signal events for the best-fit oscillation parameters from Kopp et al. [33] are indicated by the white histogram on top in each distribution.*

listed for Dirt and Cosmogenic events are larger than those given in Sections II F and II G. This is a result of energy smearing effects which are properly simulated in the final sensitivity analysis ($15\%/\sqrt{E}$), but not in the earlier stages of simulations that generate the predictions. The predicted background energy spectra are provided well below the 200 MeV cutoff value used in the analysis such that events can be properly smeared in both directions. Because both backgrounds are steeply falling functions of photon energy, more events smear into the analysis range than smear out. This is properly handled in the analysis and leads to an increase in event

TABLE IX: *Event rates in the ν_e charged-current candidate sample in the range 200–3000 MeV reconstructed neutrino energy for 6.6×10^{20} protons on target in LAr1-ND and the ICARUS T600 and 13.2×10^{20} protons on target in MicroBooNE. The numbers listed correspond to the application of topological cuts 1) & 2) for reducing cosmogenic backgrounds. In parentheses are indicated the reduced cosmogenic background rate when a 95% efficient time-based ID system is used to reject contaminated triggers. Vetoing of these events results in a reduction of all beam related event categories of 2.5%, 3%, and 5% in LAr1-ND, MicroBooNE, and ICARUS, respectively, which is not shown but is accounted for in Figure 21 and 22.*

	LAr1-ND 6.6×10^{20} p.o.t.	MicroBooNE 13.2×10^{20} p.o.t.	ICARUS T600 6.6×10^{20} p.o.t.
$\mu \to \nu_e$	6,712	338	607
$K^+ \to \nu_e$	7,333	396	706
$K^0 \to \nu_e$	1,786	94	180
NC $\pi^0 \to \gamma\gamma$	1,356	81	149
NC $\Delta \to \gamma$	87	5	9
ν_μ CC	484	35	51
Dirt events	44	47	67
Cosmogenic events[a]	156 (8)	220 (11)	204 (10)
Signal ($\Delta m^2 = 0.43$ eV^2, $\sin^2 2\theta = 0.013$) [33]	139	167	615

[a]These predictions exclude a small correction from the case where an unidentified neutrino interaction provides the scintillation trigger, as discussed in Section II G.

count relative to the earlier values which cut on generated photon energies.

Figure 22 presents the experimental sensitivity of the proposed Fermilab SBN program to $\nu_\mu \to \nu_e$ appearance signals. As discussed in Section I C, a 3+1 model is used as the basis for quantifying the sensitivity, so we present the result in the (Δm^2_{41}, $\sin^2 2\theta$) plane and compare to the original LSND allowed region [16] and two recent 3+1 global data fit results [32, 33]. Two sensitivities are shown, corresponding to the analysis with and without the additional 95% cosmic background rejection coming from timing information described above. On the left is the sensitivity with only TPC topology cuts to identify cosmogenic events, and on the right is with the additional rejection. The LSND 99% C.L. allowed region is covered at the $> 5\sigma$ level in both cases, but one sees a clear reduction in the sensitivity at low Δm^2 where oscillations occur at lower energies - exactly where cosmic backgrounds populate. While the 3+1 sensitivity seems fairly robust to this level of cosmic contamination, it is important to note that this is only in the context of a specific model and there are other motivations for taking additional measures to mitigate these backgrounds further as in the second case. The low energy region is a particularly important region to explore, especially given the anomalies reported in that region by the MiniBooNE experiment [18, 19].

The sensitivity results presented in Figure 22 incorporate all background sources and related uncertainties described in this proposal except detector related systematics as introduced in Section II E. Each of the rate predictions and other systematic uncertainties (i.e. flux and cross section) in the analysis are built using advanced, sophisticated simulation programs, while current estimates of detector related systematics come from hand scanning of events, empirical experience with these and other detectors, or toy Monte Carlo studies. Studies to

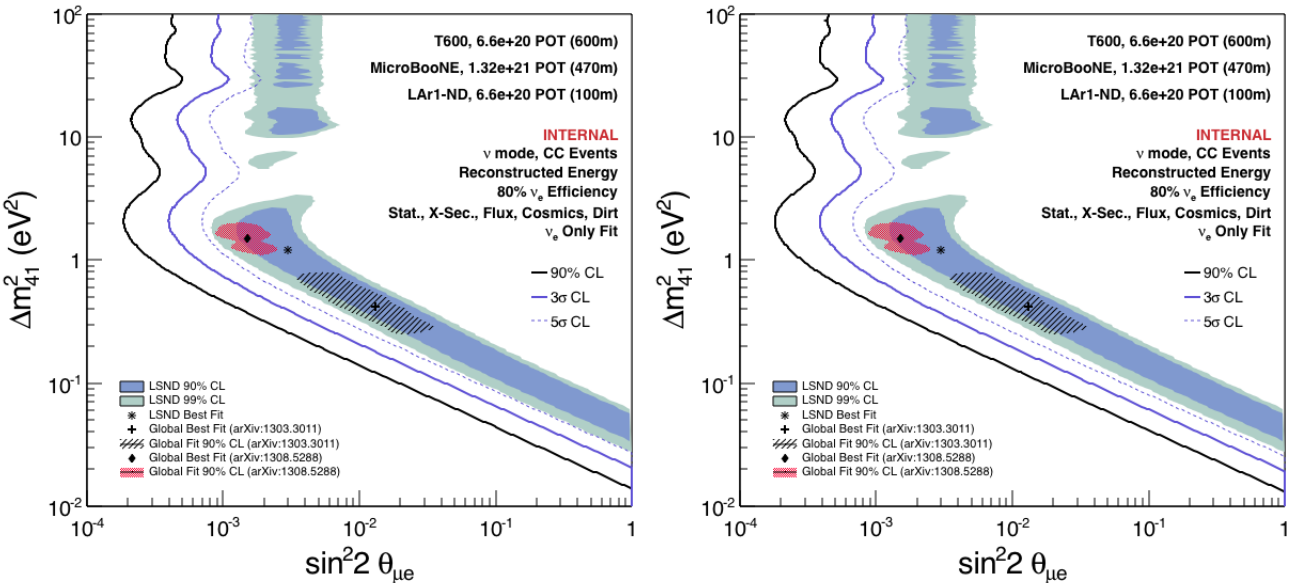

FIG. 22: *Sensitivity predictions for $\nu_\mu \rightarrow \nu_e$ oscillations including all backgrounds and systematic uncertainties described in this proposal (except detector systematics, see text). The sensitivities shown correspond to the event distributions in Fig. 21. The result on the left is using only topological information provided by the TPC to reject cosmogenic backgrounds. The result on the right includes an additional 95% rejection factor coming mainly from an external cosmic tagging system to reject muons arriving at the detector in time with the beam.*

investigate the level of uncorrelated detector systematics that can be tolerated while preserving the experimental sensitivity and the capability to cover at the 5σ level the LSND allowed parameter region have indicated that total uncertainties in the 2–3% are acceptable. All studies performed to date suggest these can be well controlled for a multi-detector experiment, with individual studies all coming in at $\leq 1\%$ (see Section II E).

Finally, in Figure 23, we present the sensitivity in a slightly different way that facilitates easier comparison between different results. Rather than plot lines of common confidence level $(90\%, 3\sigma, 5\sigma)$ in the (Δm^2, $\sin^2 2\theta$) plane, we plot the significance with which the experiment covers the 99% C.L. allowed region of the LSND experiment as a function of Δm^2. The curves in the bottom plot of the Figure are extracted by asking what χ^2 value the analysis produces at each point along the blue highlighted line in the top plot. The gray bands correspond to Δm^2 ranges where LSND reports no allowed regions at 99% C.L.

The three curves shown in Figure 23 present the significance at which the experiment covers the LSND result for the three different possible combinations of SBN detectors: LAr1-ND + MicroBooNE only (blue), LAr1-ND + ICARUS only (black), and all three detectors in combination (red). This presentation makes clear the contributions of the MicroBooNE and ICARUS T600 detectors as far detectors in the oscillation search. The presence of the large mass added by the ICARUS T600 detector is imperative to achieving $>5\sigma$ coverage, but MicroBooNE, by starting to run several years earlier, also makes a valuable contribution to the strength of the program, especially in the 1 eV^2 region.

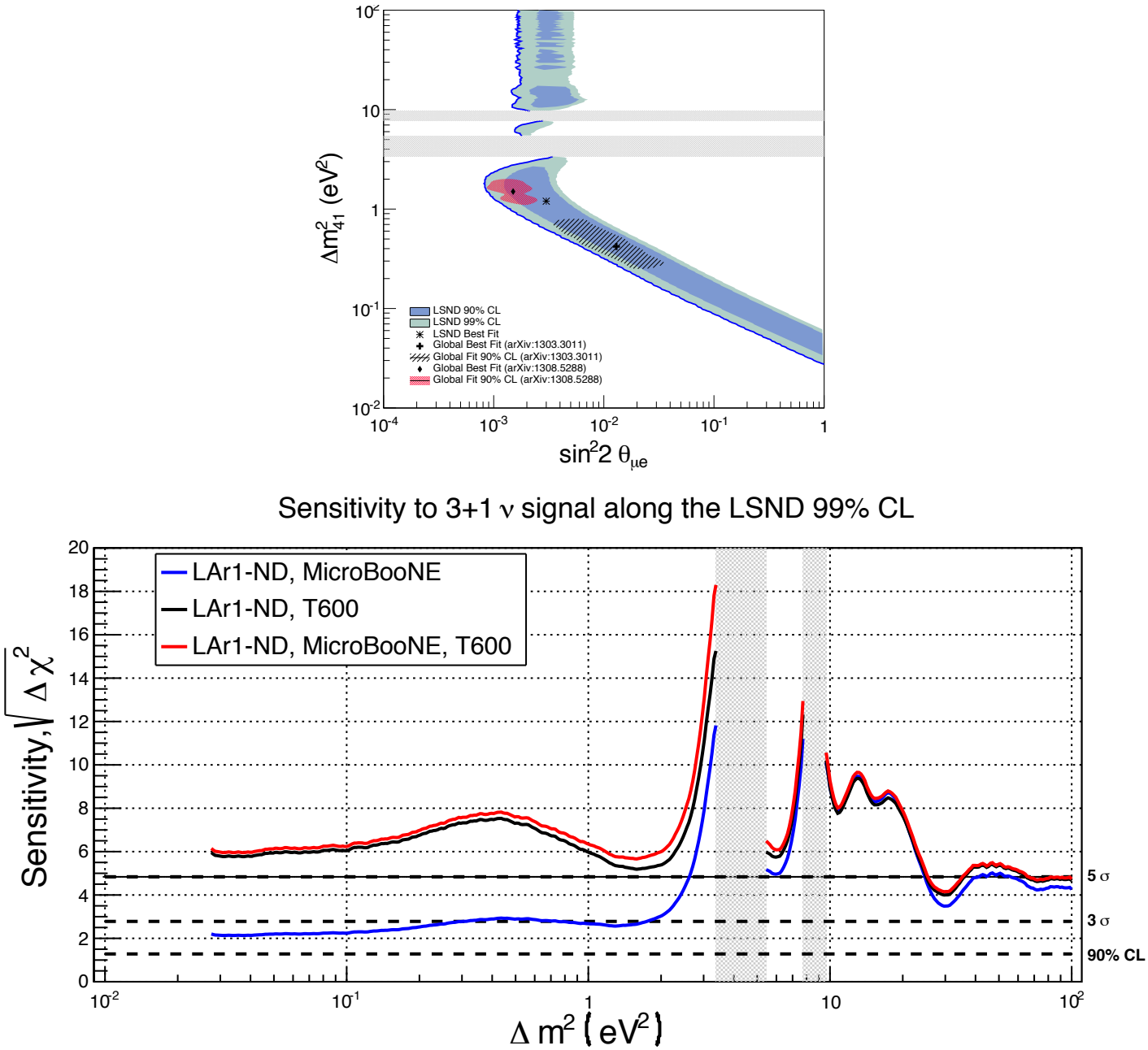

FIG. 23: *Sensitivity comparisons for $\nu_\mu \rightarrow \nu_e$ oscillations including all backgrounds and systematic uncertainties described in this proposal (except detector systematics, see text) assuming 6.6×10^{20} protons on target in LAr1-ND and the ICARUS T600 and 13.2×10^{20} protons on target in MicroBooNE. The three curves present the significance of coverage of the LSND 99% allowed region (above) for the three different possible combinations of SBN detectors: LAr1-ND + MicroBooNE only (blue), LAr1-ND + ICARUS only (black), and all three detectors (red).*

I. $\nu_\mu \to \nu_x$ Disappearance Sensitivity

The ν_μ disappearance sensitivity is not affected by the dirt or cosmogenic backgrounds discussed above. The critical aspects to this evaluation are the neutrino flux and interaction model uncertainties described in Sections II C and II D. The absolute flux and cross section uncertainties in any detector along the BNB are larger than 10%, but the high correlations between the near detector and the MicroBooNE/ICARUS T600 event samples along with the excellent statistical precision of the LAr1-ND measurements will make the SBN program the most sensitive ν_μ disappearance experiment at $\Delta m^2 \sim$1 eV^2.

Figure 25 presents the ν_μ disappearance sensitivity assuming 6.6×10^{20} protons on target exposure in LAr1-ND and ICARUS T600 and 13.2×10^{20} protons on target in MicroBooNE. The red curve is the 90% confidence level limit set by the SciBooNE and MiniBooNE joint analysis [68] and is to be compared to the solid black curve (also 90% C.L.) for the LAr SBN program presented here. Figure 24 shows two examples of $\nu_\mu \to \nu_x$ oscillation signals (for $\Delta m^2 = 0.44$ eV^2 and 1.1 eV^2) in the three detectors for the exposures given above.

The ν_μ disappearance measurement is a critical aspect of the SBN program and is needed to confirm a signal, if seen in ν_e appearance, as oscillations. Also, a genuine $\nu_\mu \to \nu_e$ appearance can be accompanied by a disappearance of the intrinsic ν_e beam component, since the three oscillation probabilities are related through a common mixing matrix. As an example, in the case of one additional sterile neutrino, $\sin^2 2\theta_{\mu e} \sim 1/4 \sin^2 2\theta_{\mu\mu} \cdot \sin^2 2\theta_{ee}$, which is valid for small mixing angles. The ability to perform simultaneous searches for oscillation signals in ν_e and ν_μ data is a major advantage for the FNAL SBN Oscillation Physics Program.

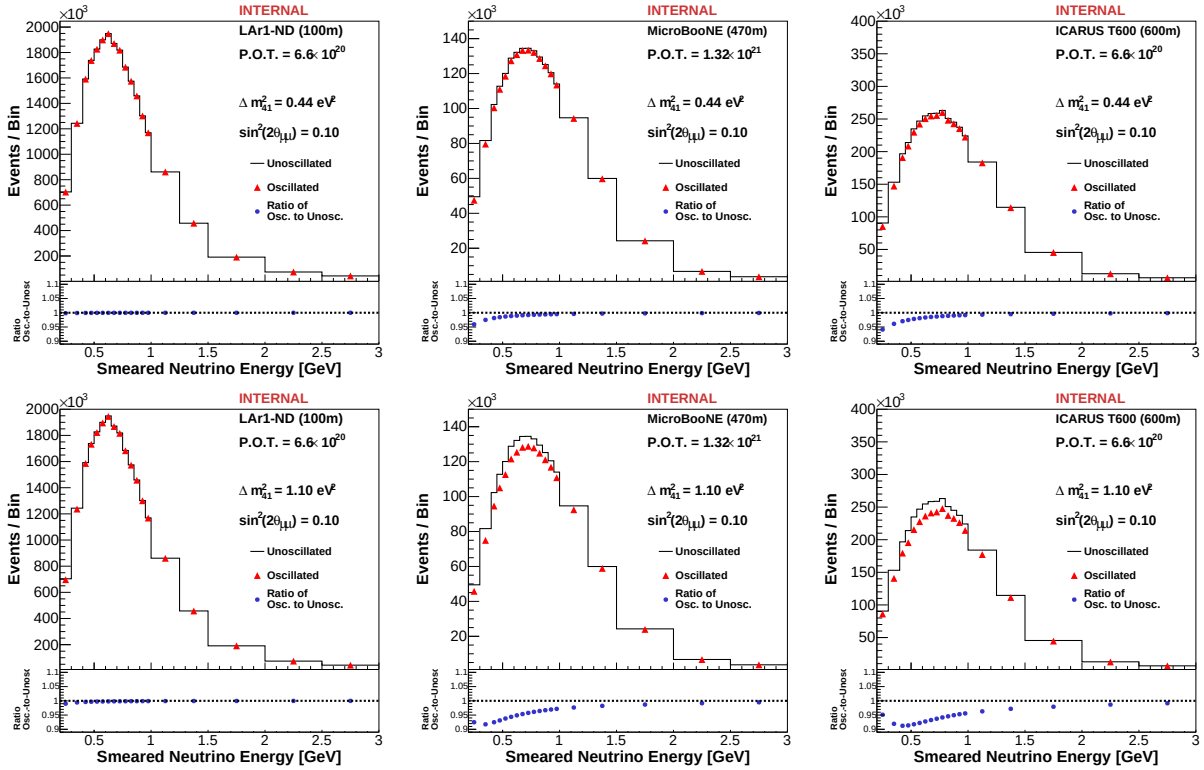

FIG. 24: *Examples of ν_μ disappearance signals in the SBN detectors for Δm^2_{41} = 0.44 eV^2 (top) and Δm^2_{41} = 1.1 eV^2 (bottom).*

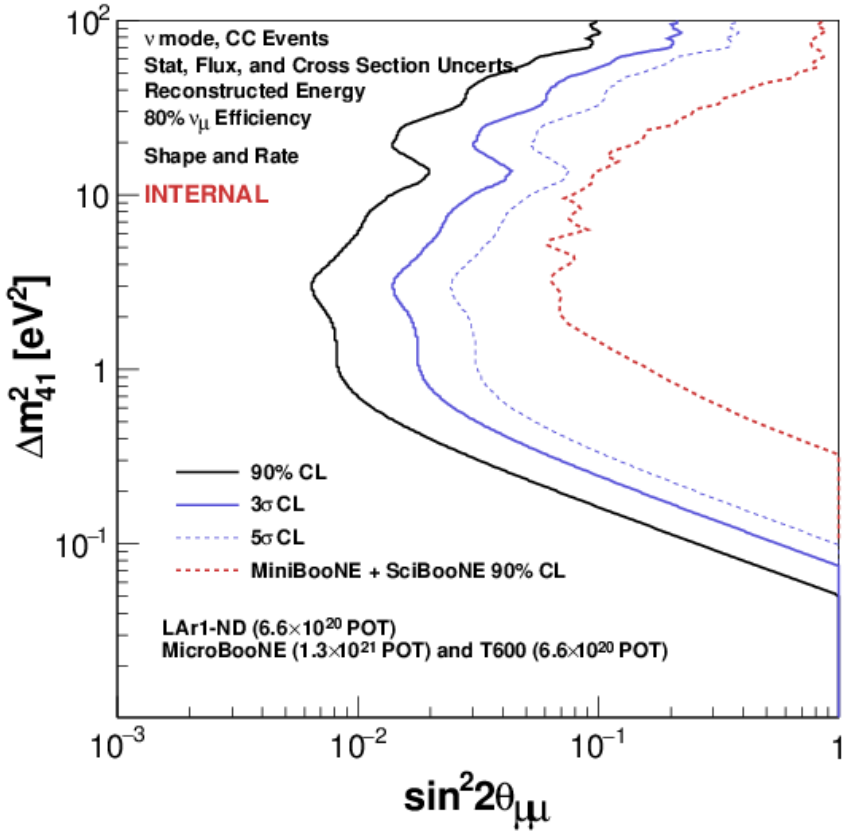

FIG. 25: *Sensitivity prediction for the SBN program to $\nu_\mu \rightarrow \nu_x$ oscillations including all backgrounds and systematic uncertainties described in this proposal (except detector systematics, see text). SBN can extend the search for muon neutrino disappearance an order of magnitude beyond the combined analysis of SciBooNE and MiniBooNE.*

Appendix A: Detector Volumes and Masses

TABLE X: *TPC active and fiducial volumes in each SBN detector used in these analyses.*

Detector volume	W (cm)	H (cm)	L (cm)	volume (m^3)	argon mass (tons)
LAr1-ND Active	2×200	400	500	80.0	112
LAr1-ND Fiducial (ν_μ analysis)	2×183.5	370	405	55.0	77.0
LAr1-ND Fiducial (ν_e analysis)	2×173.5	350	420	51.0	71.4
MicroBooNE Active	256	233	1037	61.9	86.6
MicroBooNE Fiducial (ν_μ analysis)	226	203	942	43.2	60.5
MicroBooNE Fiducial (ν_e analysis)	206	183	957	34.2	47.9
ICARUS T600 Active	4×150	316	1795	340.3	476
ICARUS T600 Fiducial (ν_μ analysis)	4×133.5	286	1700	259.6	363
ICARUS T600 Fiducial (ν_e analysis)	4×123.5	266	1715	225.4	315

[1] I. Stancu *et al.* (BooNE Collaboration), "Technical Design Report for the 8 GeV Beam," http://www-boone.fnal.gov/publicpages/8gevtdr_2.0.ps.gz (2001).

[2] I. Stancu *et al.* (BooNE Collaboration), "Technical Design Report for the MiniBooNE Neutrino Beam," http://www-boone.fnal.gov/publicpages/target_tdr.ps.gz (2001).

[3] A. Aguilar-Arevalo *et al.* (MiniBooNE Collaboration), Phys.Rev. **D79**, 072002 (2009), arXiv:0806.1449 [hep-ex].

[4] M. Catanesi *et al.* (HARP Collaboration), Eur.Phys.J. **C52**, 29 (2007), arXiv:hep-ex/0702024 [hep-ex].

[5] A. A. Aguilar-Arevalo *et al.* (MiniBooNE Collaboration), Phys. Rev. D **81**, 092005 (2010).

[6] A. Ereditato *et al.*, (2014), arXiv:1406.6400 [physics.ins-det].

[7] MicroBooNE project, "The MicroBooNE Technical Design Report," CD3b review (February 2012).

[8] T. Briese, L. Bugel, J. Conrad, M. Fournier, C. Ignarra, *et al.*, JINST **8**, T07005 (2013), arXiv:1304.0821 [physics.ins-det].

[9] C. Adams *et al.*, "LAr1-ND: Testing Neutrino Anomalies with Multiple LAr TPC Detectors at Fermilab," proposal P-1053 submitted to the Fermilab PAC in January 2014.

[10] C. Rubbia, M. Antonello, P. Aprili, B. Baibussinov, M. B. Ceolin, *et al.*, JINST **6**, P07011 (2011), arXiv:1106.0975 [hep-ex].

[11] S. Amerio *et al.* (ICARUS Collaboration), Nucl.Instrum.Meth. **A527**, 329 (2004).

[12] K. Abazajian, M. Acero, S. Agarwalla, A. Aguilar-Arevalo, C. Albright, *et al.*, (2012), arXiv:1204.5379 [hep-ph].

[13] G. Mention, M. Fechner, T. Lasserre, T. Mueller, D. Lhuillier, *et al.*, Phys.Rev. **D83**, 073006 (2011), arXiv:1101.2755 [hep-ex].

[14] W. Hampel *et al.* (GALLEX Collaboration), Phys.Lett. **B420**, 114 (1998).

[15] J. Abdurashitov *et al.* (SAGE Collaboration), Phys.Rev. **C59**, 2246 (1999), arXiv:hep-ph/9803418 [hep-ph].

[16] A. Aguilar-Arevalo *et al.* (LSND Collaboration), Phys.Rev. **D64**, 112007 (2001), arXiv:hep-ex/0104049 [hep-ex].
[17] A. Aguilar-Arevalo *et al.* (MiniBooNE Collaboration), Phys.Rev.Lett. **98**, 231801 (2007), arXiv:0704.1500 [hep-ex].
[18] A. Aguilar-Arevalo *et al.* (MiniBooNE Collaboration), Phys.Rev.Lett. **102**, 101802 (2009), arXiv:0812.2243 [hep-ex].
[19] A. Aguilar-Arevalo *et al.* (MiniBooNE Collaboration), Phys.Rev.Lett. **110**, 161801 (2013), arXiv:1207.4809 [hep-ex].
[20] T. Mueller, D. Lhuillier, M. Fallot, A. Letourneau, S. Cormon, *et al.*, Phys.Rev. **C83**, 054615 (2011), arXiv:1101.2663 [hep-ex].
[21] P. Huber, Phys.Rev. **C84**, 024617 (2011), arXiv:1106.0687 [hep-ph].
[22] Lasserre T., "(Light) Sterile Neutrinos," `https://indico.cern.ch/event/303475/contribution/11/material/slides/0.pdf` (2014).
[23] A. Hayes, J. Friar, G. Garvey, G. Jungman, and G. Jonkmans, Phys.Rev.Lett. **112**, 202501 (2014), arXiv:1309.4146 [nucl-th].
[24] A. Aguilar-Arevalo *et al.* (MiniBooNE Collaboration), Phys.Rev.Lett. **103**, 111801 (2009), arXiv:0904.1958 [hep-ex].
[25] N. Agafonova *et al.*, J.H.E.Phys. **1307**, 004 (2013), arXiv:1303.3953 [hep-ex].
[26] M. Antonello, B. Baibussinov, P. Benetti, E. Calligarich, N. Canci, *et al.*, Eur.Phys.J. **C73**, 2345 (2013), arXiv:1209.0122 [hep-ex].
[27] M. Antonello, B. Baibussinov, P. Benetti, E. Calligarich, N. Canci, *et al.*, Eur.Phys.J. **C73**, 2599 (2013), arXiv:1307.4699 [hep-ex].
[28] B. Armbruster *et al.* ((KARMEN Collaboration)), Phys. Rev. D **65**, 112001 (2002).
[29] A. Romosan *et al.*, Phys. Rev. Lett. **78**, 2912 (1997).
[30] S. Avvakumov and other, Phys. Rev. Lett. **89**, 011804 (2002).
[31] P. Astier *et al.*, Physics Letters B **570**, 19 (2003).
[32] C. Giunti, M. Laveder, Y. Li, and H. Long, Phys.Rev. **D88**, 073008 (2013), arXiv:1308.5288 [hep-ph].
[33] J. Kopp, P. A. N. Machado, M. Maltoni, and T. Schwetz, JHEP **1305**, 050 (2013), arXiv:1303.3011 [hep-ph].
[34] Lasserre T., (2014), arXiv:1404.7352 [hep-ph].
[35] A. S. Cucoanes (Nucifer Collaboration), J.Phys.Conf.Ser. **375**, 042063 (2012).
[36] K. Abazajian, M. Acero, S. Agarwalla, A. Aguilar-Arevalo, C. Albright, *et al.*, (2012), arXiv:1204.5379 [hep-ph].
[37] I. Alekseev, V. Belov, V. Brudanin, M. Danilov, V. Egorov, *et al.*, Phys.Part.Nucl.Lett. **11**, 473 (2014), arXiv:1305.3350 [physics.ins-det].
[38] A. Serebrov, V. Zinoviev, A. Fomin, U. Loginov, M. Onegin, *et al.*, (2012), arXiv:1205.2955 [hep-ph].
[39] G. Guo, F. Han, X. Ji, J. Liu, Z. Xi, *et al.*, (2013), arXiv:1303.0607 [physics.ins-det].
[40] J. Ashenfelter *et al.* (PROSPECT Collaboration), (2013), arXiv:1309.7647 [physics.ins-det].
[41] T. Lasserre, (2014), arXiv:1404.7352 [hep-ex].
[42] G. Bellini *et al.* (Borexino Collaboration), JHEP **1308**, 038 (2013), arXiv:1304.7721 [physics.ins-det].
[43] M. Cribier, M. Fechner, T. Lasserre, A. Letourneau, D. Lhuillier, *et al.*, Phys.Rev.Lett. **107**, 201801 (2011), arXiv:1107.2335 [hep-ex].
[44] A. Gando, Y. Gando, S. Hayashida, H. Ikeda, K. Inoue, *et al.*, (2013), arXiv:1312.0896

[physics.ins-det].
[45] J. Angrik *et al.* (KATRIN Collaboration), (2005).
[46] J. Formaggio and J. Barrett, Phys.Lett. **B706**, 68 (2011), arXiv:1105.1326 [nucl-ex].
[47] A. Esmaili and O. L. Peres, Phys.Rev. **D85**, 117301 (2012), arXiv:1203.2632 [hep-ph].
[48] C. Aberle, A. Adelmann, J. Alonso, W. Barletta, R. Barlow, *et al.*, (2013), arXiv:1307.2949.
[49] M. Elnimr *et al.* (OscSNS Collaboration), (2013), arXiv:1307.7097.
[50] D. Adey, S. Agarwalla, C. Ankenbrandt, R. Asfandiyarov, J. Back, *et al.*, (2013), arXiv:1305.1419 [physics.acc-ph].
[51] P. Kyberd *et al.* (nuSTORM Collaboration), (2012), arXiv:1206.0294 [hep-ex].
[52] T. Bhlen, F. Cerutti, M. Chin, A. Fass, A. Ferrari, P. Ortega, A. Mairani, P. Sala, G. Smirnov, and V. Vlachoudis, Nuclear Data Sheets **120**, 211 (2014).
[53] A. Ferrari, P. Sala, A. Fassò, and J. Ranft, *FLUKA: a multi-particle transport code*, Tech. Rep. CERN-2005-10, INFN/TC_05/11, SLAC-R-773 (CERN, 2005).
[54] G. Battistoni, A. Ferrari, M. Lantz, P. R. Sala, and G. I. Smirnov, in *CERN-Proceedings-2010-001*, pp. 387–394.
[55] I. Chemakin *et al.* (E910 Collaboration), Phys.Rev. **C77**, 015209 (2008), arXiv:0707.2375 [nucl-ex].
[56] F. Abe, K. Hara, S. Kim, K. Kondo, S. Miyashita, *et al.*, Phys.Rev. **D36**, 1302 (1987).
[57] G. Cheng *et al.* (SciBooNE Collaboration), Phys.Rev. **D84**, 012009 (2011), arXiv:1105.2871 [hep-ex].
[58] C. Andreopoulos *et al.*, Nucl. Instrum. Meth. **A614**, 87 (2010), arXiv:0905.2517 [hep-ph].
[59] C. Andreopoulos *et al.* (GENIE Collaboration), "The GENIE Neutrino Monte Carlo Generator: Physics and Users Manual," `http://genie.hepforge.org/manuals/GENIE_PhysicsAndUserManual_20130615.pdf` (2013).
[60] G. Battistoni, A. Ferrari, T. Montaruli, and P. Sala, Astroparticle Physics **17**, 477 (2002).
[61] S.Muraro, Ph.D. thesis (2006).
[62] P. Zuccon, B. Bertucci, B. Alpat, G. Ambrosi, R. Battiston, G. Battistoni, W. Burger, D. Caraffini, C. Cecchi, L. D. Masso, N. Dinu, G. Esposito, A. Ferrari, E. Fiandrini, M. Ionica, R. Ionica, G. Lamanna, M. Menichelli, M. Pauluzzi, and P. Sala, Astroparticle Physics **20**, 221 (2003).
[63] C. Hagmann, D. Lange, and D. Wright, "Monte carlo simulation of proton-induced cosmic-ray cascades in the atmosphere," `http://nuclear.llnl.gov/simulation/doc_cry_v1.7/cry_physics.pdf.` (2012).
[64] T. Gaisser, "Cosmic rays and particle physics," Cambridge University Press, 1990. isbn: 978-0521339315. (1990).
[65] M. Berger, J. Hubbell, S. Seltzer, J. Chang, J. Coursey, R. Sukumar, D. Zucker, and K. Olsen, "Xcom: Photon cross sections database," `http://www.nist.gov/pml/data/xcom/index.cfm`.
[66] C. Rubbia, (2014), arXiv:hep-ex/0702024 [hep-ex].
[67] C. Rubbia, (2014), SBN docdb 113, internal SBN report.
[68] K. B. M. Mahn, Y. Nakajima, *et al.* (MiniBooNE and SciBooNE Collaborations), Phys. Rev. D **85**, 032007 (2012).